UV Resonance Raman Investigations of Peptide and Protein Structure and Dynamics

Sulayman A. Oladepo,[†,§] Kan Xiong,[†] Zhenmin Hong,[†] Sanford A. Asher,*,[†] Joseph Handen,[‡] and Igor K. Lednev[‡]

[†]Department of Chemistry, University of Pittsburgh, Pittsburgh, Pennsylvania 15260, United States

[‡]Department of Chemistry, University at Albany, SUNY, 1400 Washington Avenue, Albany, New York 12222, United States

S *Supporting Information*

CONTENTS

1. PROTEIN FOLDING

1.1. Protein Folding Problem

An understanding of the mechanism(s) of protein folding, whereby the ribosome synthesized biopolymer folds into its native protein, is arguably one of the most important unsolved problems in biology.[1−7] The primary sequence of many or most proteins encodes both the native structure and the folding mechanism pathway to the native structure.[8−10] Over the last 50 years numerous groups have examined the mechanisms of protein folding, with a major objective being to develop methods to predict the native conformation from the primary protein sequence. An understanding of the encoded protein folding "rules" would dramatically speed insight into protein structure and function; this knowledge would result in the first principles design of drugs to treat human diseases, many of which result from protein mutations and/or from protein misfolding.

A vast theoretical and experimental literature exists on protein folding. A number of mechanisms have been proposed that differ in the order of folding events. For example, the framework model[11] and the diffusion-collision model[12] propose that the initial step in folding involves formation of native-like secondary structural units, whereas the hydrophobic collapse model[13,14] and the nucleation-condensation model[14] suggest that hydrophobic or nucleating domains fold first, and that these structures drive the subsequent formation of secondary structure. Recent energy landscape models[4,15−24] propose the occurrence of funnel-shaped folding energy landscapes, where the native state is accessed via a strategically sloped energy landscape that funnels myriads of partially folded conformations toward the native folded state.[4,25,26]

1.2. Techniques for Studying Protein Folding

It is presently impossible to perform first principle simulations of protein folding. The existing theoretical approaches are limited to the modeling of small system dynamics for very short times due to the existing limitations of computer power. The

present state-of-the-art modeling utilizes molecular dynamics (MD) with empirical or semiempirical force fields to infer structural and dynamical aspects of protein folding.[27−29] Unfortunately, computer time limitations on the time lengths of the MD simulations prevent straightforward MD calculations to achieve equilibrium structures. Thus, equilibrium structures are generally only inferred from these short MD simulations.

Numerous experimental techniques are being applied to study protein folding. UV−visible absorption spectroscopy was the first technique used to monitor the UV absorption of the peptide backbone. This method was able to detect protein backbone conformational changes because of the hypo- and hyperchromic interactions that, for example, result from peptide bond excitonic interactions in the α-helix conformation.[30,31] The development of circular dichroism spectroscopy enabled more direct monitoring of protein secondary structural content, especially the occurrence of α-helical conformations.[32,33]

X-ray crystallography is the gold standard technique for determining static protein structures. Unfortunately, its use requires the preparation of protein crystals.[34−36] Much of the insight into protein science has resulted from the many incisive stationary X-ray structures. However, these static X-ray structures do not give the dynamic structural information essential to determine enzymatic mechanisms, for example. The X-ray structure is used as a basis to infer dynamics. The further the structure of an activated complex from the static structure, the more speculative will be the inference.

Nuclear magnetic resonance spectroscopy (NMR) is an extraordinarily powerful tool for studying protein folding.[37−39] It can be applied to studying both static structures, as well as protein and peptide dynamics. The technique is also capable of elucidating detailed aspects of the structure and dynamics of large proteins. However, the atomic distances and dihedral angles measured by this technique are generally time averages.[39] In addition, NMR requires significant measurement time and may require sophisticated isotope labeling. Although, methods based on MD simulation and solid-state NMR have been recently developed for the determination of protein conformational distribution in the backbone peptide bonds,[40,41] information on the distribution of distances and angles about the mean values are crucial for understanding important biological phenomena such as protein folding. Thus, there is a need for spectroscopic methods that give additional insight to investigate protein folding and dynamics.

Optical and especially laser spectroscopy techniques enable highly incisive structural investigations that can be utilized to study dynamics in the fsec to static time scales. IR and Raman vibrational spectroscopies can monitor small changes in protein structure resulting from tiny ∼0.001 nm bond length changes. Unfortunately, the use of IR absorption spectroscopy is challenging for biological samples, because it is generally limited to D_2O solution samples due to the overwhelming IR absorption of H_2O.[42]

2. UV RESONANCE RAMAN SPECTROSCOPY

2.1. UV Resonance Raman Scattering

Raman vibrational spectroscopy monitors the vibrations of gas, liquid, and solid samples.[43−45] H_2O is a relatively weak Raman scatterer, which enables Raman studies of biological molecules in water. Raman spectroscopy is an inelastic light scattering phenomenon where the incident electromagnetic field interacts with a molecule such that there is an exchange of a quantum of vibrational energy between the two, resulting in a
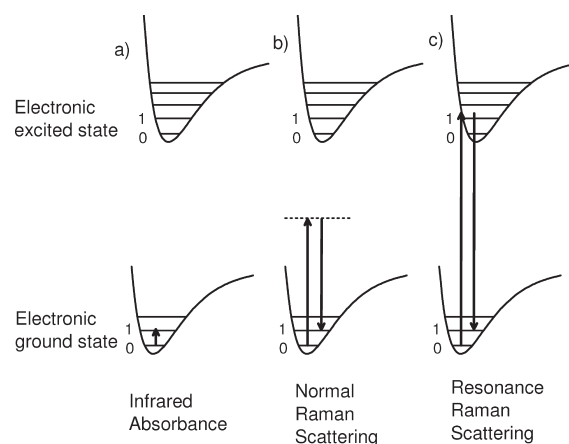

Figure 1. Comparison of infrared absorption, normal Raman scattering, and resonance Raman scattering.

vibrational frequency difference between the incident and scattered light.

The theory of Raman scattering has been well-described in the literature.[46−55] Figure 1 compares the IR absorption and Raman scattering phenomena. In IR absorption (Figure 1a), a molecule absorbs a photon with an energy matching the vibrational energy difference between two energy levels of a particular molecular vibration. Generally, the molecule undergoes a transition from the $\nu = 0$ vibrational ground state to the $\nu = 1$ excited vibrational level.

In normal, or off-resonance, Raman scattering (Figure 1b), the incident photon that is at a frequency outside of any electronic absorption band is inelastically scattered, leaving the molecule in an excited vibrational level of the electronic ground state (for Stokes scattering). An identical vibrational transition occurs for resonance Raman scattering, where excitation occurs at a frequency within an electronic absorption band (Figure 1c). In this case the vibrational modes observed are particular vibrations whose motions couple to the driven electronic motion occurring in the electronic transition. The vibrational modes enhanced are those localized in the chromophoric segments. The resonance Raman cross sections are much larger than the nonresonance Raman cross sections.

As for any light scattering process from objects significantly smaller than the wavelength of light, the Raman intensities increase approximately with the fourth power of the excitation frequency. The additional *resonance* Raman enhancement can be an additional $10^6−10^8$-fold. This results in a crucial ultrahigh resonance Raman selectivity and sensitivity that makes it a very powerful technique for studying macromolecules. Instead of all the sample vibrations contributing with comparable intensities, only a small set of resonance Raman enhanced vibrations localized around the chromophoric group dominate the spectra.

Judiciously tuning the excitation wavelength allows for selectively enhancing a particular vibration in particular regions of the macromolecule.[56,57] Figure 2 demonstrates the UV resonance Raman (UVRR) selectivity available, for example, for studying the protein myoglobin (Mb).[58,59] The visible wavelength absorption bands of Mb result from the in-plane $\pi \rightarrow \pi^*$ electronic transitions of its heme group. UVRR excitation of Mb at 415 nm in the strong heme Soret absorption band results in an intense UVRR spectra, which contains only the in-plane heme ring vibrations.[60,61] In contrast, excitation at 229 nm within the absorption bands of the tyr and trp aromatic side chains shows UVRR spectra completely dominated by tyr and trp aromatic ring
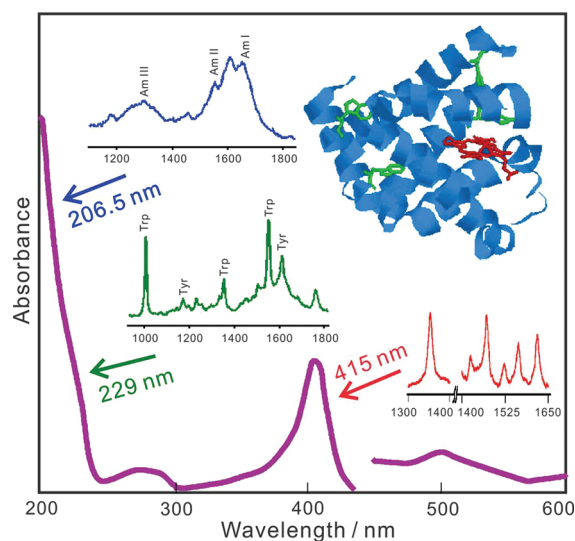
Figure 2. Selectivity of resonance Raman spectral measurements of myoglobin showing the protein absorption spectrum and the different resonance Raman spectra obtained with different excitation wavelengths.

side-chain vibrations.[62] Deeper UV excitation at 206.5 nm, within the $\pi \rightarrow \pi^*$ transitions of the amide peptide bonds, shows UVRR spectra dominated by the peptide bond amide vibrations.[59]

Thus, tuning the UVRR excitation wavelengths allows the probing of different chromophoric segments of a macromolecule. Another advantage of deep UV Raman measurements is that there is no interference from molecular relaxed fluorescence because those chromophores that have their first transition below 260 nm are highly flexible and possess vanishingly small fluorescence quantum yields.[63] In addition, UVRR can also be used in pump−probe measurements to give kinetic information on fast biological processes.[64,65] Thus, UVRR is a powerful technique for studying static protein structure and for studying protein dynamics, such as, for example, in protein folding.

2.2. UVRR Instrumentation

The rapid development of UVRR has been aided by recent advances in lasers, optics, and detectors. Figure 3 shows the schematic diagram of a typical back-scattering UVRR instrument that can be used for static and kinetic studies.[66−69] For temperature-jump (T-jump) measurements, an IR pump pulse at 1.9 μm excites the overtone absorption band of water and heats a small sample volume. A time-delayed UV probe pulse excites the UVRR of the IR pulse-heated volume. The UVRR light is collected and dispersed by a spectrograph, and the spectrum is detected by a charge-coupled device (CCD) detector. Nonkinetic Raman measurements of static structure are best measured by using CW lasers that avoid nonlinear optical processes and thermal processes that can induce sample degradation.[70−72]

However, high repetition rate (1−5 kHz) pulsed (10−50 ns) Nd:YLF pumped Ti:Sapphire lasers[67,73] are very convenient UVRR laser sources because their output can be easily and continuously tuned between 193 and 240 nm. These deep UV excitation beams are generated by frequency quadrupling or tripling and mixing the Ti:Sapphire laser fundamentals.

UVRR measurements generally flow the sample through the excitation beam as shown in Figure 3 to avoid sample heating and accumulation of photochemical degradation products. Excitation of an open sample stream also avoids any interfering
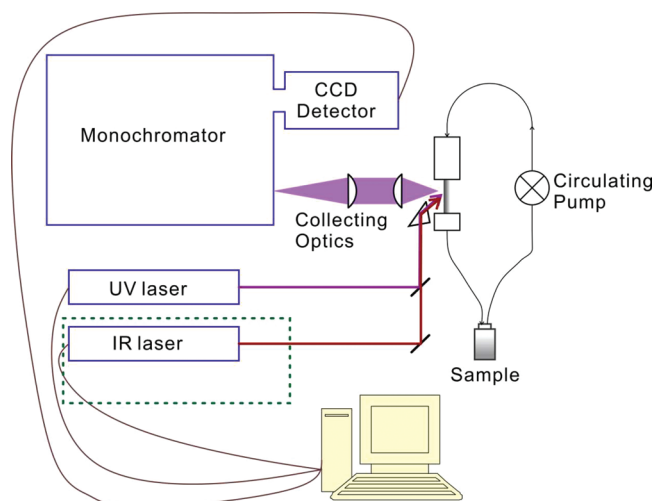
Figure 3. Schematic diagram of a typical back-scattering UVRR instrument, which utilizes an IR laser to achieve T-jump kinetic measurements.
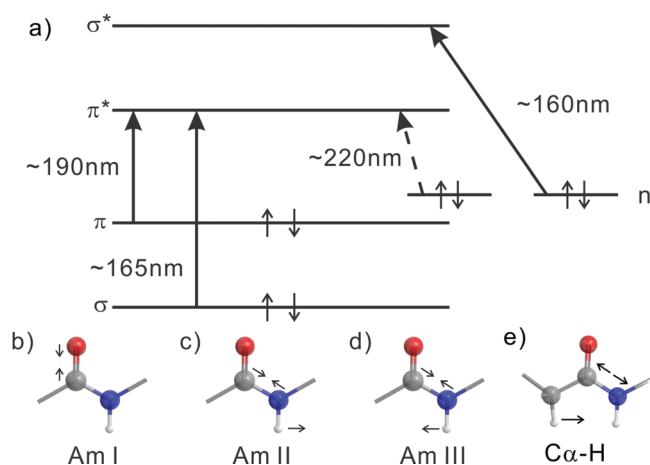
Figure 4. (a) HOMO and LUMO orbitals of peptide bonds in peptides and proteins and (b−e) UVRR enhanced peptide bond vibrational modes.

Raman signals from sample cell walls.[74] If the sample volume is limited, a spinning silica capillary or cuvette with a magnetic stir bar can be used to contain the sample.[67,75]

Liquid-nitrogen-cooled CCD cameras are the optimum UVRR detectors because of their low noise. At present the best S/N comes from CCD cameras with fluorophore coatings to convert the UV light into the visible, where the CCD detector has high quantum efficiencies.

3. PROTEIN AND PEPTIDE BOND STUDIES

Figure 4a shows the highest occupied (HOMO) and lowest unoccupied (LUMO) molecular orbitals of the peptide bond (secondary amide group, except for proline). The lowest energy n $\rightarrow \pi^*$ transition at ∼220 nm is electronically forbidden and weak. It gives rise to the strong circular dichroism (CD) signature of the α-helix conformation but gives rise to negligible RR enhancement.[76,77] The ∼190 nm $\pi \rightarrow \pi^*$ transition is strongly allowed, with a strong absorption band that gives rise to strong UVRR intensities.[78] This electronic transition results in a significant expansion of the C−N bond with a smaller expansion of the

carbonyl bond. Excitation within this absorption band gives rise to the strong UVRR enhancement of vibrations that have large components of C−N stretching. A somewhat smaller enhancement occurs for vibrations with a large component of C=O stretching.[79]

Parts b−e of Figure 4 show the UVRR peptide bond vibrations enhanced. Excitation at ~200 nm gives rise to strong UVRR intensities for particular peptide bond vibrations,[75,80−84] which include the following: the Amide I (AmI) vibration (~1660 cm^{-1}) that consists mainly of C=O stretching and a small amount of out-of-phase C−N stretching; the Amide II (AmII) vibration (~1550 cm^{-1}) that consists of an out-of-phase combination of CN stretching and NH bending motions; and the Amide III (AmIII) vibration (between ~1200 and 1340 cm^{-1}), which is a complex vibration involving C−N stretching and NH bending. A C_α−H_b vibration that contains significant C_α−H bending (~1390 cm^{-1}) is also enhanced if the peptide bond conformation enables C_α−H bending motion to couple to C−N stretching.[85]

These UVRR enhanced peptide bond vibrations (except for the AmI) derive from vibrational modes localized within individual peptide bonds. The AmI vibrations show small couplings between adjacent peptide bonds.[80,86,87] The local mode character of the Am II, AmIII, and C_α−H bending peptide bond vibrations allows the measured UVRR spectrum to be modeled as the linear sum of contributions of the individual peptide bond UVRR spectra.[81]

This enabled Asher and co-workers to develop a quantitative methodology to determine protein secondary structure directly from the measured UVRR spectra.[88] They measured the UVRR spectra of a set of proteins with known X-ray structures and calculated the "basis" spectra of the three major secondary structure motifs: α-helix, β-sheet, and unfolded conformation.

Figure 5 shows the basis spectra of the α-helix, β-sheet, and unfolded structures obtained as discussed previously. The pure α-helix spectrum shows an AmI band at 1647 cm^{-1}, an AmII band at 1545 cm^{-1}, an AmIII band at ~1299 cm^{-1}, and no C_α−H bending band. The pure β-sheet spectrum shows an AmI band at 1654 cm^{-1}, an AmII band at 1551 cm^{-1}, an AmIII band at 1235 cm^{-1}, and the C_α−H bending band at 1386 cm^{-1}. The unfolded structure (now known to be PPII) spectrum shows an AmI band at 1665 cm^{-1}, an AmII band at 1560 cm^{-1}, an AmIII band at 1267 cm^{-1}, and a C_α−H bending band at 1386 cm^{-1}.[88] The fractional secondary structure composition of a protein with an unknown secondary structure can be uniquely determined by linearly fitting these basis spectra to the protein UVRR spectra. The fitted weighting fractions are the fractional amounts of each secondary structure motif.[88]

3.1. UVRR Excitation Profiles

RR excitation profiles, which display the dependence of the resonance Raman cross sections on the excitation wavelength, detail the magnitude of coupling of vibrations to the electronic transitions underlying the absorption band envelope. UVRR excitation profile measurements and measurements of the wavelength dependence of the Raman depolarization ratios (ρ) provide information on the underlying electronic transitions that are responsible for the broad complex absorption bands. Figure 6 shows the UVRR spectra of the α-helix and the melted, PPII conformations of a 21-residue mainly ala peptide (AP) of sequence AAAAA(AAARA)$_3$A excited between 218 and 194 nm.[77] The relative intensities of the Raman bands increase
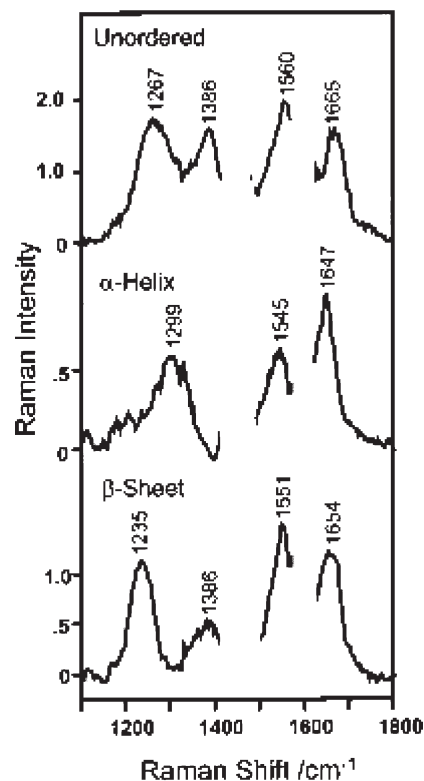

Figure 5. Pure secondary structure UVRR basis spectra obtained from a library of protein UVRR spectra. The regions around 1610 and 1450 cm^{-1} are excluded because their spectral conformational dependence is not completely understood. Adapted with permission from ref 88. Copyright 1998 American Chemical Society.

as the excitation wavelength decreases from 218 to 194 nm. The UVRR excitation profiles of different conformations differ, as do their UVRR spectra as discussed in detail below.[77] The UVRR cross sections for the PPII-like conformation are approximately twice those of the α-helical conformation (for λ > 200 nm, Figure 7) due to the hypochromism that results from the excitonic interactions between the α-helical peptide bond electronic transitions.

The α-helix and the melted PPII conformations also show different excitation profile maxima, indicating shifts in absorption band maxima between the underlying electronic transitions. A shoulder seen in the excitation profiles (Figure 7) around 206 nm suggests an additional underlying electronic transition, which is confirmed by the complex dispersions of the depolarization ratios, which otherwise would have a value ρ = 0.33 if derived from a single nondegenerate electronic transition.[46,77] In a related study,[89] the excitation profiles of tri- and tetraalanine peptides revealed 202 nm charge transfer electronic transitions, where electron transfer occurs from the terminal nonbonding carboxylate orbital to the adjacent peptide bond π^* orbital,[89] as observed previously for glycylglycine.[90] From this work it is clear that there presently exists only a modest understanding of the UV electronic transitions of peptide bonds.

3.2. Correlation Between Spectral Features And Protein Secondary Structure

The UVRR spectra of proteins and peptides are conformationally sensitive as shown in Figure 8, which describes the UVRR study of α-helix melting of poly-L-glutamic acid (PGA) at pH 4. PGA is α-helical at low temperatures but melts to unfolded
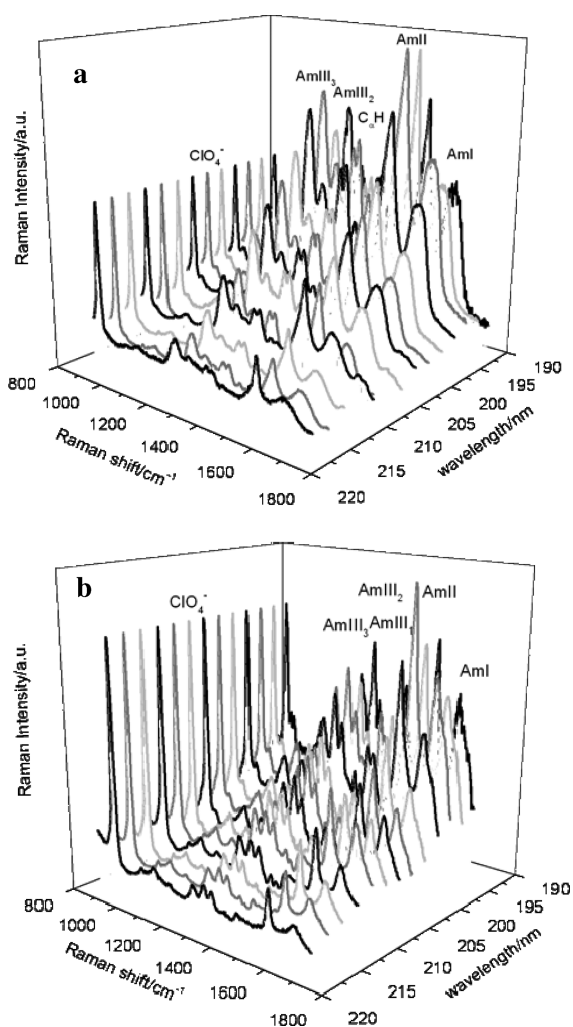
Figure 6. (a) Observed UVRR spectra between 218 and 194 nm of AP in a PPII-like conformation at 60 °C. (b) UVRR spectra between 218 and 194 nm of α-helix conformation of AP at 5 °C obtained by subtracting the appropriate amount of PPII UVRR spectrum at each excitation wavelength. Both sets of spectra show similar but not identical enhancement patterns. All spectra were normalized to the 932 cm^{-1} ClO$_4^-$ internal standard. Adapted with permission from ref 77. Copyright 2008 American Chemical Society.

Figure 7. Absolute Raman cross sections excitation profiles between 194 and 218 nm for (a) PPII-like conformation and (b) α-helix conformations of AP. (c) UV–vis absorption spectrum of AP at 5 °C, where it is predominantly α-helical, and at 60 °C, where it is in a predominantly PPII-like conformation. Inset: Structure of AP. Adapted with permission from ref 77. Copyright 2008 American Chemical Society.

structures at high temperatures.[91] The α-helix low-temperature UVRR spectrum shows an AmI band at ~1647 cm^{-1}, an AmII band at ~1560 cm^{-1}, a (C)C$_\alpha$–H bending band (also called the Am S band by some workers) at ~1390 cm^{-1}, and AmIII bands between ~1200 and ~1340 cm^{-1}. As the temperature increases, the AmI band upshifts from ~1647 to ~1670 cm^{-1} and becomes broader, while the AmII band downshifts from ~1560 to ~1555 cm^{-1}. These results indicate weakened hydrogen bonding (HB) with increasing temperature. Previous work showed that the water HB to the peptide bond C=O increases the C=O bond length and, thus, downshifts the AmI band, whereas water HB to the peptide bond N–H upshifts the AmII band.[92] Thus, the extent of HB partially determines the UVRR band frequencies (see a discussion of different HB patterns below).

The C$_\alpha$–H intensity increase with temperature indicates α-helix melting.[85,88] The α-helix conformation shows a negligible C$_\alpha$–H bending band intensity, in contrast to the unfolded

extended conformation that has a high C$_\alpha$–H bending intensity.[85,88]

The AmIII region contains three sub-bands: AmIII$_1$, AmIII$_2$, and AmIII$_3$. However, only two of these sub-bands are clearly resolved in the AmIII region of PGA: the AmIII$_2$ band (~1303 cm^{-1}) and the AmIII$_3$ band (~1250 cm^{-1}). The AmIII$_3$ band (which is most sensitive to conformation) derives from motions that involve coupling of NH bending to C$_\alpha$–H bending and CN stretching.[83,93] As the temperature increases, the melted polyproline II (PPII)-like conformation increases and the corresponding unfolded PPII AmIII$_3$ band (~1247 cm^{-1}) in PGA becomes more prominent, overshadowing the low-temperature α-helical AmIII$_3$ band. This clearly signals melting of the α-helix conformation to a PPII conformation.
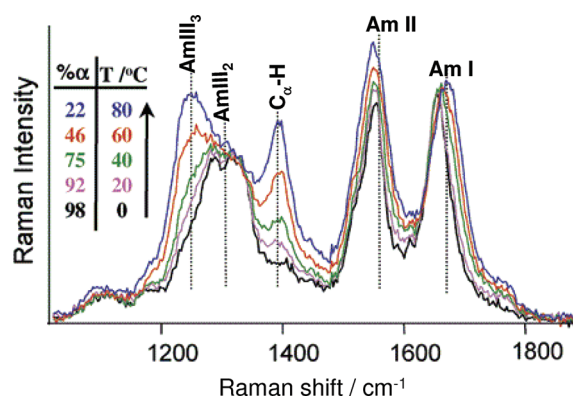
Figure 8. Temperature dependence of the UVRR spectra and resulting α-helix fractions of poly-L-glutamic acid at pH 4.3 calculated from the UVRR spectra. Adapted with permission from ref 91. Copyright 2001 American Chemical Society.

Figure 9. Relative orientations of N–H and C_α–H bonds in the polyproline II and α-helix conformations.

Figure 10. Correlation between AmIII$_3$ frequency, peptide bond HB pattern, and Ramachandran Ψ angle: (□) measured AmIII$_3$ frequencies of α-helix, antiparallel β-sheet, PPII, and 2.5$_1$-helix in aqueous solution; (◇) measured AmIII$_3$ frequencies of peptide crystals, plotted against their Ψ angles: 1, Ala-Asp; 2, Gly-Ala-Leu·3H$_2$O; 3, Val-Glu; 4, Ala-Ser; 5, Val-Lys; 6, Ser-Ala; 7, Ala-Ala. Blue curve is the predicted correlation (eq 1) for full HB to water (PPII, 2.5$_1$-helix, and extended β-strand); green curve is a theoretically predicted correlation for two end-on peptide bond–peptide bond HBs (α-helix-like conformation and interior strands of β-sheet); magenta curve is the predicted correlation for a peptide bond where only the C=O group has peptide bond–peptide bond HB (three α-helix N-terminal peptide bonds and half of peptide bonds of the exterior strands of β-sheet); black curve is the predicted correlation for a peptide bond with just their N–H group peptide bond involved in peptide bond–peptide bond HB (three α-helix C-terminal peptide bonds and half that of peptide bond of exterior strand of β-sheet). Adapted with permission from ref 82. Copyright 2006 American Chemical Society.

The large AmIII$_3$ band frequency conformational dependence derives from the fact that coupling between C_α–H bending and N–H bending peptide bond motions depends sensitively on the peptide bond Ramachandran Ψ dihedral angle that, in part, defines the peptide bond secondary structure conformation.[82,91] The Asher group discovered a sinusoidal dependence of the AmIII$_3$ frequency on this Ramachandran Ψ angle.[82,91] Conveniently, they also found little dependence of the AmIII$_3$ frequency on the other dihedral angle, the Ramachandran Φ angle (for sterically allowed Ψ angles).[94] The origin of this Ψ angle frequency difference between the α-helix and extended conformations results from the fact that the α-helix peptide bond conformations have *trans* N–H and C_α–H bonds that prevent coupling (Figure 9). Thus, the α-helix AmIII$_3$ frequency occurs at 1258 cm^{-1} and the C_α–H bending band contains negligible C–N and N–H bending motion and is, thus, not resonance-enhanced.

In contrast, peptide bonds adopting an extended PPII-like conformation have *cis* N–H and C_α–H bonds whose motions couple well. The AmIII$_3$ band frequency downshifts to 1245 cm^{-1}, and the C_α–H bending vibration contains C–N stretching and N–H bending motion resulting in resonance enhancement.[82] Quantitative relations were determined that relate the AmIII$_3$ band frequencies to Ramachandran Ψ angles for different peptide bond HB states.[82]

For example, for peptide bonds fully hydrogen bonded to water such as in PPII, 2.5$_1$-helix, and extended β-strand conformations:

$$\nu_{AmIII_3}^{EXT}(\Psi, T) = 1256 \text{ cm}^{-1} - 54 \text{ cm}^{-1} \sin(\Psi + 26°)$$
$$- 0.11 \frac{\text{cm}^{-1}}{°\text{C}} T \qquad (1)$$

where T is temperature. The family of quantitative relationships determining the AmIII$_3$ frequencies ignore the more modest Ramachandran Φ angle dependencies.[94]

This family of equations allows estimation of the Ψ angle for the different possible peptide bond HB states. The estimated error of this determination was suggested to be ≤ ±14°.[82] Figure 10 shows the family of theoretical curves that correlate the AmIII$_3$ frequencies to the Ramachandran Ψ angles for the different HB states.[82] As shown below, correlating the inhomogeneously broadened AmIII$_3$ band shape to the underlying Ramachandran Ψ angle distribution enables the determination of the peptide bond conformatio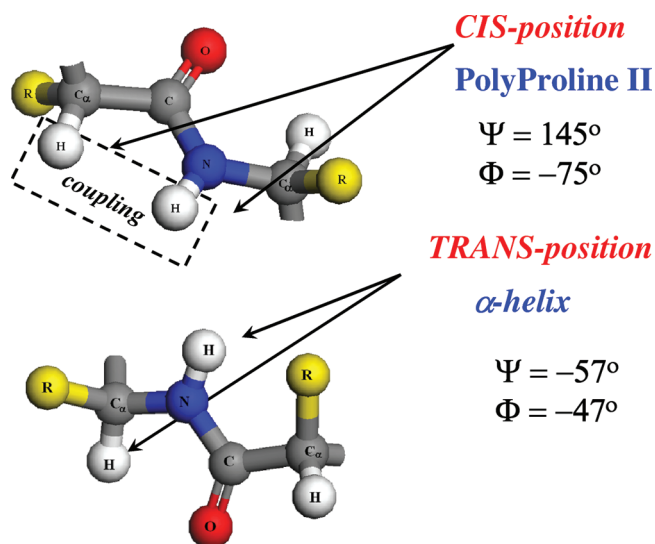nal distributions in peptides and proteins. Most importantly, these conformational distributions can be used to calculate the Gibbs free energy landscapes along the Ψ angle coordinates, which are the most important (un)folding reaction coordinates.

Figure 11. Frequency distribution of AmIII$_3$ band calculated by deconvolution of homogenously broadened AmIII$_3$ band profiles of XAO of the sequence Ac-XXAAAAAAAOO-NH$_2$ (A is alanine, O is ornithine, X is diaminobutyric acid), A$_5$–A$_3$ (ala$_5$-ala$_3$), non-α-helical AP of the sequence AAAAA-(AAARA)$_3$A, acid-denatured apomyoglobin, and the frequency distribution of spectra of a library of proteins. The resulting histogram shows the population distribution underlying the measured AmIII$_3$ bands. Adapted with permission from ref 95. Copyright 2004 American Chemical Society.

3.3. Protein Folding Energy Landscapes

The UVRR spectra show inhomogeneously broadened bands that reflect the distribution of conformations experienced by the protein. In the case of the AmIII$_3$ band, the inhomogeneous distribution reflects mainly the distribution of peptide bond Ψ angles and HB states.

Asher and co-workers assumed that the experimentally measured, inhomogeneously broadened AmIII$_3$ band, $A(\nu)$, derives from the sum of M Lorentzian bands, which result from the different peptide bond conformations with different band frequencies, νe_i. The AmIII$_3$ band homogeneous line width, $\Gamma = 7.5$ cm^{-1}, was determined from UVRR measurements of small peptide crystals in defined secondary structure states.[95]
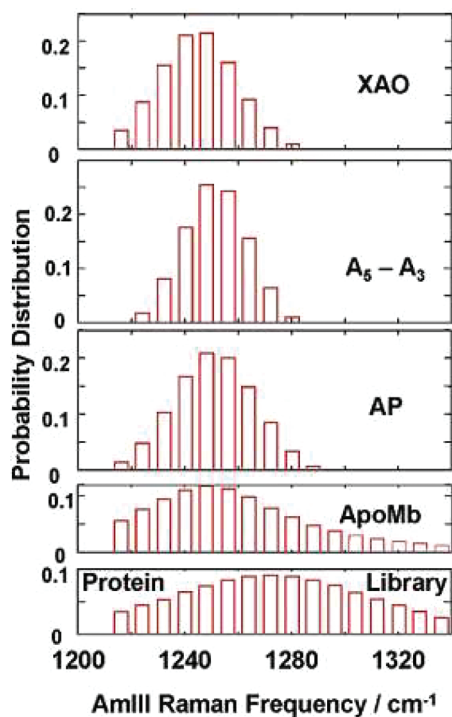
$$A(\nu) = \pi^{-1} \sum_{i=1}^{M} L_i \cdot \frac{\Gamma^2}{(\nu - \nu e_i)^2 + \Gamma^2} \qquad (2)$$

where L_i is the probability for the contributing band to occur at frequency νe_i.

Asher and co-workers deconvoluted out the homogeneous line width from the peptide bond UVRR spectrum to calculate the underlying inhomogeneously broadened AmIII$_3$ band shape.[95] Figure 11 shows histogram plots of the calculated underlying AmIII$_3$ band frequency distributions for a set of peptides and proteins. The XAO peptide of sequence Ac-XXAAAAAAAOO-NH$_2$ (A is alanine, O is ornithine, and X is diaminobutyric acid) is known to be primarily in a PPII conformation.[96] As shown in
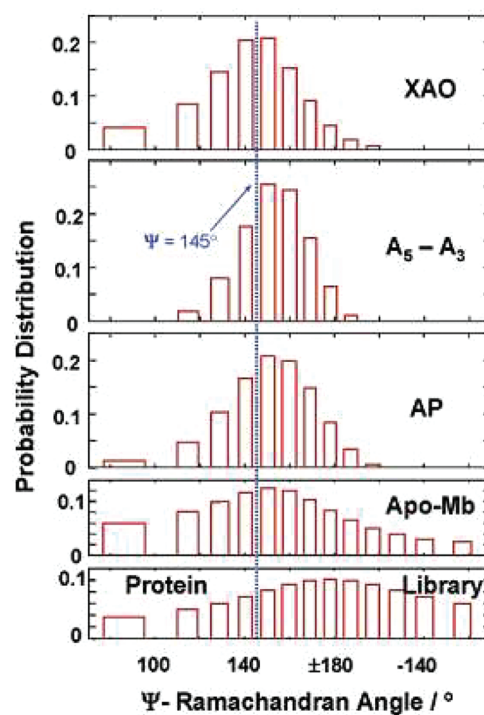
Figure 12. Estimated Ramachandran Ψ angle distribution of XAO, A$_5$–A$_3$, non-α-helical AP, acid-denatured apomyoglobin, and "disordered" protein conformations. Adapted with permission from ref 95. Copyright 2004 American Chemical Society.

Figure 11, the XAO frequency distribution is similar to that of A$_5$–A$_3$ (the difference UVRR between ala$_5$ and ala$_3$ that models the spectrum of the interior A$_5$ peptide bonds), indicating that these peptide bonds predominantly populate the PPII conformation, as do the peptide bonds of the AP peptide (primarily polyala) at elevated temperature. Acid-denatured apomyoglobin shows a broad frequency distribution, as expected, from its distribution of conformations. The "protein library", of course, shows the broadest frequency distribution.

Asher and co-workers used eq 1, relating the AmIII$_3$ band frequency to the Ramachandran Ψ angle, to convert the frequency distributions to Ψ angle distributions (Figure 12). Further, by applying the Boltzmann relation to the Ψ angle distributions, the relative Gibbs free energy along the Ramachandran Ψ angle coordinate can be calculated, since the population at any particular Ψ angle is determined by its relative Gibbs free energy.[97]

For example, this approach was used to determine the Gibbs free energy landscape (Figure 13) for poly-L-lysine (PLL). At neutral and low pH values, PLL adopts extended conformations that include the PPII and 2.5$_1$-helix conformations. The 2.5$_1$-helix conformation results from the PLL charged side-chain electrostatic repulsions.[97,98] Ma et al.[99] used UVRR to monitor the temperature and NaClO$_4$ concentration dependence of the PLL Gibbs free energy landscape (Figure 13). They observed an α-helix-like basin containing α-helix and π-bulge conformations and a basin containing extended PPII and 2.5$_1$-helix conformations.

As indicated in Figure 13, adding NaClO$_4$ induces a change from a solution equilibrium between extended PPII and 2.5$_1$-helix conformations, to an equilibrium involving α-helix-like conformations.[99] This conformational change results from charge screening due to strong ion-pair formation between ClO$_4^-$ and the lysine

2610

dx.doi.org/10.1021/cr200198a |Chem. Rev. 2012, 112, 2604–2628
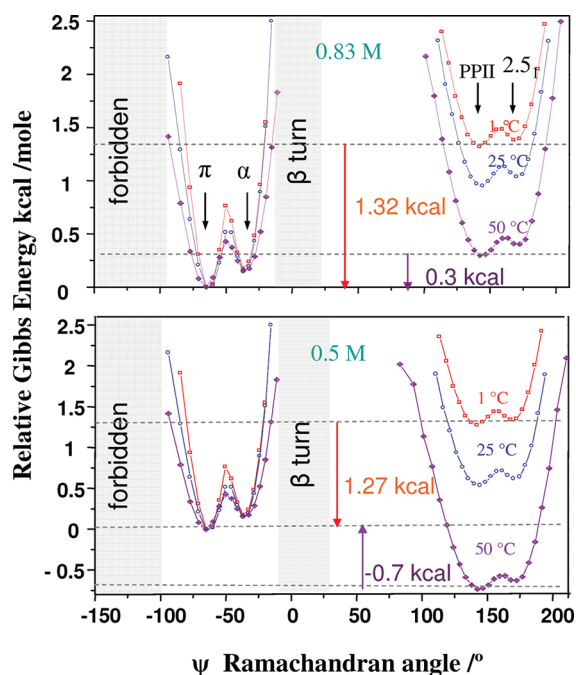
Figure 13. Estimated Gibbs free energy landscape for poly-L-lysine in 0.83 and 0.5 M NaClO$_4$ at 1, 25, and 50 °C. Increasing the NaClO$_4$ concentration from 0.5 to 0.83 M stabilizes α-helix-like conformations. Higher temperatures stabilize the unfolded conformations. Adapted with permission from ref 99. Copyright 2007 American Chemical Society.

side chain $-NH_3^+$, which reduces the repulsion between charged side chains. Figure 13 also shows that increasing temperatures cause the α-helix-like conformations to melt to extended conformations.

3.4. T-Jump Kinetic Studies of Protein Folding

Dynamic UVRR measurements can be used to elucidate biomolecular structural dynamics.[54] T-jump experiments monitored by UVRR measurements can elucidate the evolution of peptide and protein secondary structure.[42,69,84,100-109] These studies probe the mechanism of structural evolution between different secondary structural motifs such as α-helix, 3$_{10}$-helix, π-bulge, and PPII conformations.[42,84,100-103,110] The rates of these transitions occur in the 100 ns to ~2 μs time regime.

Recent ns to μs protein folding dynamics studies found complex unfolding behaviors. For example, recent studies of the AP peptide melting demonstrate a complex pathway that involves melting of multiple α-helix-like structures, which include the 3$_{10}$-helix, π-bulge, and pure α-helix conformations, that have different melting curves to the PPII-like unfolded conformation.[82,84,101,111]

To gain insight into the dynamics of protein (un)folding, the Asher group constructed the first T-jump UVRR spectrometer that they used to examine conformational relaxation subsequent to ns T-jumps.[84,101] The peptide and protein relaxation after the T-jump utilizes folding and unfolding conformational change coordinates that are easily studied with UVRR. These T-jumps used ~5 ns excitation pulses at 1.9 μm that occur within a water vibrational overtone absorption band. Thermalization of the absorbed energy occurs within 70 ps.[112,113] It is easy to achieve ~20 °C T-jumps from the ~5 ns IR laser pulses.

In their first kinetic studies, the Asher group examined the kinetics of melting of the AP peptide that at low temperature is mainly α-helical.[101] Steady-state measurements discussed above showed that the α-helix melts to a PPII conformation. Figure 14A shows the T-jump relaxation transient difference UVRR spectra of AP in H$_2$O and D$_2$O. The transient difference spectra measured at delay times as long as 1 μs were modeled using a linear combination of α-helix and the PPII equilibrium UVRR basis spectra. The first spectral changes evident at <10 ns derive from fast HB changes of water bound to the peptide bonds in the PPII state due to the temperature increase.[100]

Subsequent relaxation spectral changes result from peptide bond conformation changes. Modeling of the transient spectra can determine the kinetics of the AP structural relaxation. Depending on the initial temperature, unfolding time constants between 180 and 240 ns were observed. By assuming a two-state model, they calculated a folding time constant of ~1 μs (Figure 14).[84,100,101]

They also observed a puzzling peculiarity in the temperature dependence of the folding and unfolding rate constants that they calculated from the relaxation rates by assuming a two-state system (which was fully consistent with the observed single exponential relaxation behavior). As the temperature increased, they calculated that the folding rate constant decreased, indicating a negative activation energy of -4^{+3}_{-2} kcal/mol, that indicates an anti-Arrhenius behavior.[101] Obviously, this peculiarity must result from the fact that the conformational transition is not two-state.

Subsequently, Mikhonin and Asher identified the additional states involved in the melting transition.[111] They found that they could spectrally differentiate α-helix-like conformational substates from the AmIII$_3$ band frequency distribution.[111] They calculated the α-helix-like UVRR spectrum by subtracting off the pure PPII UVRR spectrum measured at higher temperature (after accounting for the temperature dependence of the PPII UVRR spectrum). Figure 15 shows calculated Ramachandran Ψ angle distributions in AP between 0 and 30 °C.

At low temperatures, the Ψ angle distribution of the α-helix-like state is broad and spans the Ψ angles of the pure α-helix, 3$_{10}$-helix, and π-helix bulge conformations. As the temperature increases, the α-helix-like Ψ angle distribution narrows until, at 30 °C, the distribution becomes very narrow and centered at $-42°$, the Ψ angle of the pure α-helix.

Figure 16 shows the melting curves determined for these different α-helix-like conformations by assuming identical Raman cross sections for the pure α-helix, the 3$_{10}$-helix, and the π-bulge conformations. T_m was determined to be 45, 20, and 10 °C for the α-helix, 3$_{10}$-helices, and π-bulges, respectively.

The anti-Arrhenius behavior observed by Lednev et al.'s T-jump measurements directly results from these different T_m for the 3$_{10}$-helix, π-bulge, and pure α-helix conformations.[107] As the temperature increases the pure α-helix conformation increasingly dominates the equilibrium conformational distribution. Apparently, the folding rate of the pure α-helix conformation is slowest. These studies clearly show the utility of UVRR to gain crucial insight into the complex nature of peptide folding dynamics.

In a recent protein T-jump study, Spiro and co-workers[104] examined the early events in the unfolding of apomyoglobin using both 197 and 229 nm excitations. These excitations allowed them to probe both the aromatic side chains and the peptide backbone conformations. Aromatic amino acid side-chain UVRR bands can monitor the solvent exposure, whereas the peptide bond UVRR bands report on backbone Ramachandran Ψ angles, as discussed previously. Measuring both spectral bands can answer the question of whether solvent exposure of the protein core precedes or follows secondary structure changes.
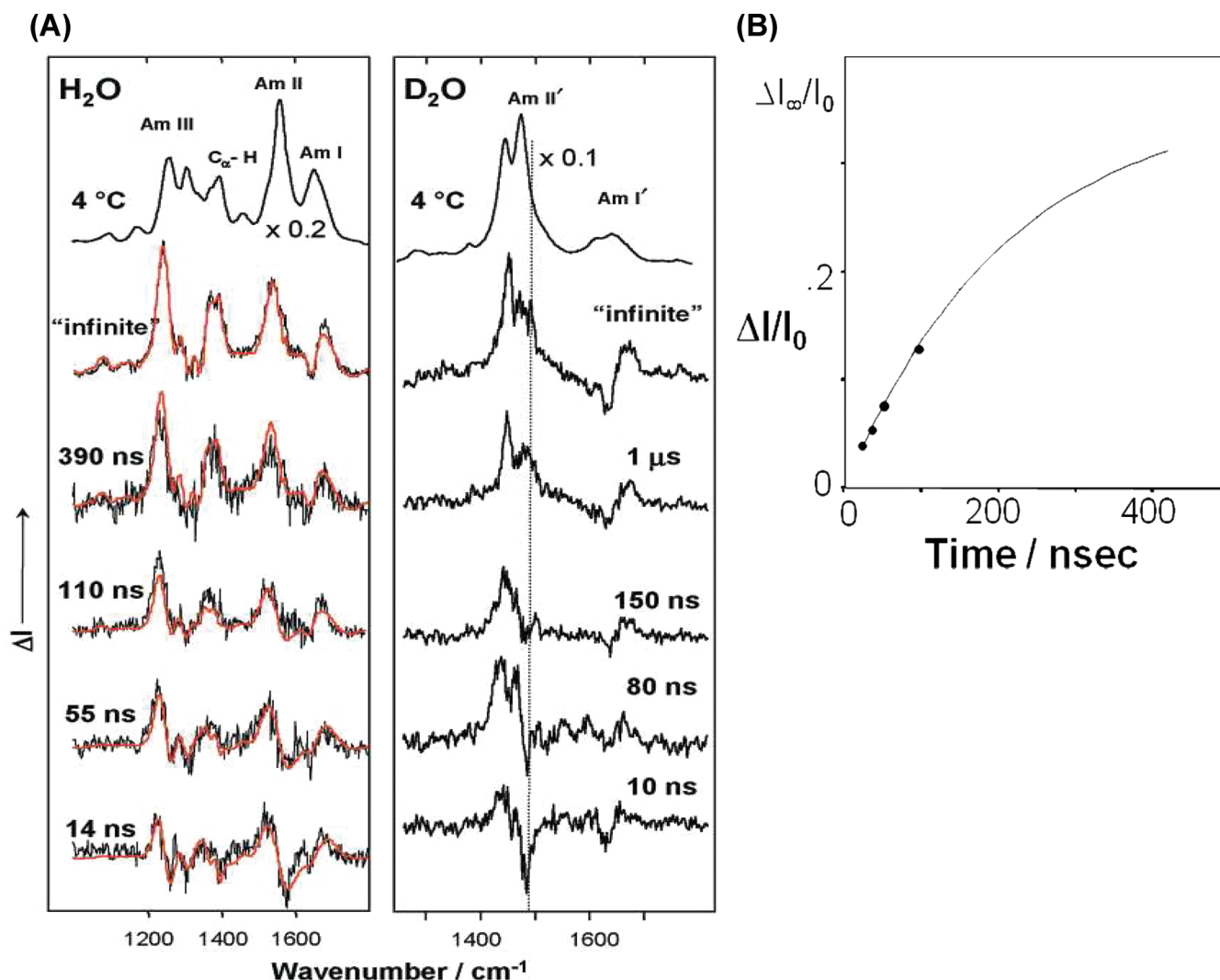
(A)

(B)

Figure 14. (A) AP UVRR spectra measured in water and D_2O solution at 4 °C (top), and transient difference spectra of AP in solution initially at 4 °C measured at different delay times following a T-jump of ~31 °C (~22 °C in D_2O). (B) Kinetics of thermal denaturation of AP. The ordinate axis is the relative change in the UV Raman intensity at 1236 cm^{-1} obtained from transient difference spectra of Figure 14 of ref 84. The abscissa is the time delay at which the spectra were acquired following the T-jump. (A) Adapted with permission from ref 100. Copyright 2001 American Chemical Society. (B) Adapted with permission from ref 84. Copyright 1999 American Chemical Society.

The authors were able to clearly differentiate the order of these events. They found that the Trp14 bands respond twice as fast as does the peptide bond α-helix melting. Thus, the Trp14 that is originally buried in the protein core becomes exposed to solvent, prior to melting of the protein core.

In another T-jump study,[106] the Spiro group found two relaxation time constants of 0.2 and 15 μs for a truncated version of the GCN4 coiled-coil peptide. They interpreted that their UVRR spectra revealed two different α-helical AmIII bands at 1340 and 1300 cm^{-1} that melt at 10 and 40 °C, respectively. The authors argued that these two bands and their different time constants reflect the melting of hydrated and unhydrated helices in the folded polypeptide chain. This is the first report of the differentiation of hydrated and unhydrated helices from UVRR.[106]

The Spiro group also found two distinct kinetic phases for the melting of the α-helical peptide (AcGSPEAAAKAAAAKAAAA-CO-D-R-CONH$_2$).[105] They observed a prompt loss of helicity (within the ~40 ns time resolution of the experiment), whose amplitude increased with the increasing final T-jump temperature,

T_f. With a constant initial temperature, T_i, the amplitude of the fast phase is initially small for small T-jumps, but increases as T_f increases from 18 to 61 °C. However, when T_i is raised in parallel with T_f, the fast phase merged into the slow phase (120 ns). They claimed that this merging of fast and slow phases is due to the shifting distribution of initial helix lengths from longer to shorter helices as the $T_i - T_f$ range shifts to higher temperatures. These two relaxation phases were attributed to a fast disruption of HB followed by slower peptide bond conformational changes. The fast (~40 ns) conformational change kinetics are quite surprising. Understanding these apparently complex dynamics will require additional studies.

3.5. Isotope-Labeling Enables Monitoring of Secondary Structure Spatial Distributions

Ianoul et al. used UVRR to examine the spatial dependence and the thermodynamics of α-helix melting of deuterium-labeled AP (AdP).[110] In AdP, all the ala residues except the four central ones were selectively deuterated. They found that melting of the

Figure 15. Calculated Ramachandran Ψ probability distributions for AP at (A) 0 °C, (B) 10 °C, (C) 20 °C, and (D) 30 °C. Adapted with permission from ref 111. Copyright 2006 American Chemical Society.

Figure 16. Melting curves for AP "α-helix-like" conformations. ($\times$) Original "α-helix" melting curve as reported by Lednev et al. (refs 83 and 98), which is a sum of individual α-, π-, and 3_{10}-helical melting curves; (red diamond) pure α-helix melting; (green square) 3_{10}-helix (type III turn) melting; (blue circle) π-helix (bulge) melting. Adapted with permission from ref 111. Copyright 2006 American Chemical Society.

isotopically labeled exterior peptide bonds could be spectrally resolved from the central ones, thus allowing the spatial resolution of the peptide bond conformational changes. The UV Raman spectra of AP and AdP at 5 °C are compared in Figure 17A. Figure 17B shows that the central residues are essentially 100%

Figure 17. (A) 204 nm UVRR spectra of AdP ($\mathbf{A_dA_dA_dA_dA_dA_dA_d}$-RAAAA-R-$\mathbf{A_dA_dA_dA_d}$-R-$\mathbf{A_dA_d}$; the bold letters label the 2,3,3,3-deuter-ated ala residues) and AP (AAAAAAAA-RAAAA-R-AAAA-R-AA); (B) The temperature dependence of α-helical fractions of the central peptide bonds and exterior peptide bonds normalized to the number of peptide bonds of the central and external segments that can form α-helices. (A) Adapted with permission from ref 107. Copyright 2007 American Chemical Society. (B) Adapted with permission from ref 110. Copyright 2002 American Chemical Society.

α-helix-like at 0 °C with a T_m of 32 °C whereas the exterior residues are ~60% α-helix-like at 0 °C with a T_m of 5 °C.

For a 5−30 °C T-jump, the central peptide bonds show a ~2-fold slower relaxation time of 189 ns, compared to 97 ns for the exterior peptide bonds.[107] However, for a 20−40 °C T-jump, the central peptide bond relaxations are faster (56 ns) than those of the exterior peptide bonds (131 ns). Assuming a two-state transition, only the exterior peptide bonds show anti-Arrhenius behavior; the central peptide bonds show normal Arrhenius-like folding and unfolding.

They ascribed the anti-Arrhenius folding behavior of the exterior peptide bonds to the involvement of π-bulges/helices and 3_{10}-helix states in unfolding.[107] Because these α-helix-like motifs have a lower T_m than that of the pure α-helix,[111] a large relative contribution from lower temperature-melting 3_{10}-helices and π-bulges/helices should give fast relaxation kinetics for the lower temperature T-jump. A large relative contribution from the higher-melting pure α-helix conformation should give slower relaxation kinetics. Hence, the authors explained that the central peptide bonds show a ~2-fold slower relaxation kinetics in the 5−30 °C T-jump, because of a higher contribution to the relaxation by the slower pure α-helix relaxation compared to that of the exterior peptide bonds (27% vs −3%). For the 20−40 °C T-jump, the central peptide bonds show faster relaxation kinetics because of the lower contribution to the relaxation by the slower pure α-helix relaxation compared to the exterior peptide bonds (7% vs 35%). The small relative contribution of the pure α-helix conformation to the central peptide bonds results in a faster relaxation.

The results obtained from this work are obviously complex. The authors argued that the results can only be understood by assuming that one of the AdP termini has a higher pure α-helix propensity than the center and the other terminus. They proposed that the pure α-helix is most stabilized at the N-terminus where eight consecutive ala occur rather than at the middle and C-terminus.[107] This study clearly shows that UVRR can spatially resolve the melting dynamics of peptides and proteins.

3.6. UVRR of Side Chains as Spectral Monitors of Protein Structure

Aromatic amino acid side-chain chromophores show strong UVRR spectra upon 229 nm excitation (Figure 2). UVRR aromatic amino acid studies have been extensively used to monitor different aspects of protein structure. For example, Hashimoto et al. used UVRR excitation at 229 nm to examine the acid-induced unfolding intermediates of sperm whale apomyoglobin and metmyoglobin.[114] They monitored the W3 and W7 band changes associated with Trp7 and Trp14 residues to probe the pH-dependent structural protein changes. They found that the unfolding of myoglobin is accompanied by a significant decrease in environmental hydrophobicity around the Trp residues. They also found that the fully unfolded form partially refolds in the presence of sulfate ions.[114] Their results also suggest a two-step transition from the native to the unfolded conformation for both proteins. These results are consistent with the two unfolded intermediates found earlier for horse apomyoglobin by Chi and Asher.[115] They argued that the transition from the native form to the unfolding intermediate results from an increased water exposure of Trp14 that is close to the E-helix. This conclusion is based on a previous report by Hughson et al. that the intermediate form of apomyoglobin has an unfolded E-helix.[116] However, this conclusion contrasts with the increased water exposure of Trp7 identified by Chi and Asher,[115] which was also corroborated by Haruta and Kitagawa's time-resolved UVRR experiments.[117]

In a pH-jump kinetic UVRR study, Haruta and Kitagawa characterized the kinetic folding intermediates of horse apomyoglobin (h-apoMb) using a rapid mixer.[117] Similar to Hashimoto's kinetic study, they monitored changes in W3 and W7 bands of Trp7 and Trp14. The pH-dependence of the intensity ratio of the W7 doublet (I_{1358}/I_{1338}) indicates the presence of two transitions, a transition between the native and equilibrium intermediate state and a transition between the equilibrium intermediate and unfolded states. In addition, analysis of their measured 244 nm excited UVRR spectra at different delay times following a pH-jump from pH 2.2 to pH 5.6 reveals three folding intermediates, I_1, I_2, and I_3. They found that the first intermediate formed before the earliest delay time of 0.25 ms. They were able to detect this intermediate by observing an upshift in the W3 band from 1553 to 1557 cm^{-1} at 0.25 ms after acid unfolding.

They rationalized this observation from experiments with a model peptide of the A-helix in water and in helix-forming solvents (e.g., trifluoroethanol/methanol/water mixture). The W3 band occurs at 1552 and 1555 cm^{-1} in water and in helix-forming solvents, respectively. They therefore concluded that I_1 involves the incorporation of Trp14 into the α-helix from the acid-induced random coil. The second intermediate, which formed 1 ms after the start of refolding, indicates decreased water exposure whereby the surroundings of Trp7 and Trp14 are hydrophobic. The third intermediate appeared at $\sim$3 ms. From the I_{1358}/I_{1338} versus time plot, the hydrophobicity of the system

at this stage is equal to that obtained for a pH 4 equilibrium intermediate. They also found that an upshift in the W3 band frequency did not occur even 40 ms after the pH-jump. Thus, they concluded that the transition from I_3 to the native state took >40 ms, indicating a slow process. This kinetic study presents a direct observation of the structural and environmental changes in the Trp side chain of h-apoMb in its early stage of refolding from an almost completely unfolded structure.

In another study, Sato and Mizutani used time-resolved UVRR spectroscopy to probe the structural dynamics of myoglobin following carbon monoxide (CO) dissociation.[118] Their ps transient UVRR spectra showed transient intensity changes for the Trp W18, W16, and W3 bands and the Tyr Y8a band that resulted from changes in the heme structure upon CO dissociation. They argued that out-of-plane motion of iron following CO dissociation induces protein motion such as E- and F-helical movements. They observed decreased intensities for these Trp and Tyr bands within 5 ps of CO dissociation. They explained that this decreased intensities resulted from rapid movement of both E- and F-helical segments. The occurrence of decreased intensity within 5 ps implies that the concerted EF-helical movement following CO dissociation is ultrafast.[118] The myoglobin protein response due to CO dissociation is demonstrated in this study.

Kim's research group examined the folded and unfolded states of the wild-type bacterial outer membrane protein A (OmpA) and two OmpA mutants.[119] Using 230 nm excitation, they studied these proteins in the absence of urea (folding condition) and in the presence of urea (unfolding condition). Under in vitro folding and unfolding conditions, they probed the Trp and Tyr side chain environments to monitor OmpA folding and unfolding. On the basis of changes in the W7 doublet intensity ratio (I_{1361}/I_{1340}) as well as shifts in W3 and W17 bands, they found that an OmpA mutant (W57 OmpA) is folded in vescicles and in detergent but unfolded in phosphate buffer. This work presents a UVRR spectral investigation of an integral membrane protein that is folded in a synthetic bilayer vesicle and uses the changes in the Trp and Tyr environments to delineate structural protein changes.

El-Mashtoly et al. used UVRR spectroscopy to examine the Trp and Tyr bands to probe the structural changes that accompany the photocycle of the photoactive yellow protein (PYP).[120] PYP is a bacterial blue light photoreceptor. Photoexcitation of its dark state (PYP$_d$) triggers a photocycle that involves a number of intermediate states that leads to the formation of the putative signaling state (PYP$_m$). With 225−250 nm UV excitation, the authors observed shifts and intensity changes in Tyr Y8a and Y9a bands that they attributed to HB changes between the Tyr42 and the chromophore in PYP$_m$. They also observed a decreased intensity of the Trp W3, W16, and W18 bands upon PYP$_m$ formation. These decreases in intensity were ascribed to an increased water exposure of the only Trp in PYP (Trp119) that is located >10 Å from the protein's active site. They therefore concluded that these observed changes suggest global protein structural changes during the transition from PYP$_d$ to PYP$_m$.[120] The study gives structural insight into the photocycle of the bacterial blue light photoreceptor, PYP.

The Mathies research group used picosecond time-resolved UVRR spectroscopy to probe the structural dynamics of rhodopsin.[121] In this study, they used a pump−probe apparatus consisting of a 1 kHz Ti:Sapphire laser system that provides <3 ps pump (466 nm) and probe (233 nm) pulses. They monitored

2614

dx.doi.org/10.1021/cr200198a | *Chem. Rev.* 2012, 112, 2604–2628

Trp and Tyr spectral features to probe rhodopsin structural changes following photon absorption. With 233 nm probe pulses, they observed a decreased Raman intensity in the Trp W3, W16, and W18 bands at zero time delay between pump and probe events. However, at longer time delays, they found that both the Trp W1, W3, W16, and W18 bands and the Tyr (Y1 + 2xY16a Fermi doublet, Y7a, and Y8a) bands showed decreased intensities. These intensity changes were attributed to a decreased hydrophobicity of the microenvironment of at least one Trp and one Tyr. Examination of the rhodopsin crystal structure suggests that W265 and Y268 are responsible for the observed UVRR spectral changes. These spectral changes are nearly identical to those observed for the transition in rhodopsin to the 1 ms intermediate (Meta I). These similarities suggest that Trp and Tyr spectral changes that lead to Meta I are initiated very early in the process, perhaps 200 fs following photon absorption. They therefore concluded that the Trp and Tyr structural changes in rhodopsin dynamics were initiated as early as 200 fs into the photoisomerization process. This study gives temporal glimpses into the structural changes that accompany the primary photochemical event in vision.

The Mathies group also carried out time-resolved UVRR experiments to characterize the structural changes that take place in the photochemical reaction cycle of bacteriorhodopsin.[122] This study carried out with 239.5 nm excitation showed Trp W1, W3, W16, and W18 intensity decreases and an upshift in the Tyr Y8b band in their 10 ns transient difference spectra. These observed spectral changes suggested that the photoisomerization of retinal from all-trans to 13-cis changes the structure and environment of aromatic residues that line the retinal binding pocket within 10 ns following photon absorption. This study reveals that UVRR spectroscopy can give insight into the early part of the photochemical cycle of membrane proteins such as bateriorhodopsin.

Barry and co-workers used pump—probe UVRR to study the roles of Trp and Tyr in electron transfer in photosystem II (PSII) in the photosynthesis process.[123,124] They used 633 nm light to initiate the photochemistry and 244 and 229 nm light to probe the conformations of Trp and Tyr. They observed light-induced Tyr radical $Z^{\bullet}$ and/or Tyr radical $D^{\bullet}$ intermediates, as well as plastoquinone anions Q_A^- and Q_B^- during electron transfer in PSII.

Okishio et al. used 235 nm UVRR excitation to probe the effect of tyrosine phosphorylation in Src-peptides (RRLIEDNEYTARG and TSTEPQYQPGENL).[125] Upon tyrosine phosphorylation, they observed that the Y8a band downshifts from 1615 to 1611 cm^{-1} while the Y7a' band downshifts from 1250 to 1240 cm^{-1}. They also observed a diminished intensity of the Y1 band at ~850 cm^{-1} and the appearance of the Y13 band at ~760 cm^{-1}. When they dephosphorylated the initially phosphorylated peptides with alkaline phosphatase (an enzyme that removes phosphates from proteins), they found that the phosphorylation-induced changes disappeared. Thus, UVRR spectroscopy can be used to delineate structural changes caused by protein phosphorylation and other protein modifications.[125]

3.7. Other UVRR Protein Studies

The Spiro group used UVRR spectroscopy to establish quantitative signatures of protein secondary structure via least-squares fitting,[74] following the example of the method reported by Chi et al.[88] They used 197 and 206.5 nm excitation to probe the peptide bonds of a set of 12 proteins with varied secondary structure contents. Their UVRR spectra show significant intensities for Phe and Tyr side chains, with small contributions from Trp side chains. They subtracted off the side-chain contributions using UVRR spectra of the pure aromatic amino acids. The resulting corrected protein spectra were then used to compute pure secondary structure spectra of β-turn, α-helix, β-sheet, and unordered structures via least-squares fitting. They illustrated the utility of their procedure by using the computed pure secondary structure spectra to determine the different secondary structural motifs in the temperature-dependent spectra of apomyoglobin. The computed pure secondary structure spectra enabled this determination.

JiJi and co-workers used the correlation optimized wrapping (COW) method to remove the overlapping water bands in the AmI region of UVRR spectra.[126] They also used constrained multivariate curve resolution-alternating least-squares (MCR-ALS) analysis[127] and parallel factor (PARAFAC) analysis[126] to resolve discrete protein secondary structural motifs.

Halsey and co-workers used UVRR spectroscopy to study membrane protein secondary structure and membrane—protein interactions.[128,129] In their work, they measured multiwavelength excited UVRR spectra of a lipid solubilized membrane protein, the Rhodobacter capsulatus cytochrome bc_1 complex (cyt bc$_1$). They observed that the AmI band intensity of cyt bc$_1$ increases dramatically compared to an aqueous soluble protein with similar secondary structure content. This was ascribed to dehydration of the backbone amides in the lipid. Deuterium-exchange experiments confirmed that the spectral changes derived from the transmembrane α-helical portion of the protein complex.

UVRR spectroscopy was also used to gain insight into the structure of Barnase, a monomeric protein of 110 residues.[130] In their work, Couling et al. used 244 nm excitation to excite Barnase in order to monitor Tyr band changes to probe changes in the protein structure that occur upon folding into its native state. By using p-cresol as a reference, they calibrated the change in the intensity ratio of the Tyr doublet I_{830}/I_{850} in terms of the Tyr HB strength and obtained a linear relationship between the doublet relative intensity ratio and the HB enthalpies of formation.

UVRR was employed by Pieridou and Hayes to determine the pK_a of Tyr, as a peptide side chain and as the free amino acid.[131] They used 239.5 nm excitation for the selective enhancement of the two Tyr residues in an 11-residue peptide fragment from transthyretin (TTR(105—115)) and monitored changes in Tyr Y8a band at different pHs. By monitoring the shifts in this band, they measured a titration curve that they fitted to a modified form of the Henderson—Hasselbach equation. They found that the pK_a of the Tyr in the peptide (10.2) are slightly higher than that of aqueous Tyr monomer (9.1). They explained that the N-terminal Tyr 105 is easily exposed to solvent, and its response to pH changes is similar to that of free Tyr. Tyr 114, on the other hand, may be involved in different HB interactions with neighboring amino acid side chains and the peptide backbone. Thus, it is possible that these two Tyr residues sample two slightly different microenvironments in the peptide with the pK_a of 10.2, representing an average value of the two Tyr.

4. UVRR STUDIES OF PROTEIN AND PEPTIDE FIBRILLATION

Protein fibrillation is often associated with human diseases such as Alzheimer's, for example. The fact that numerous
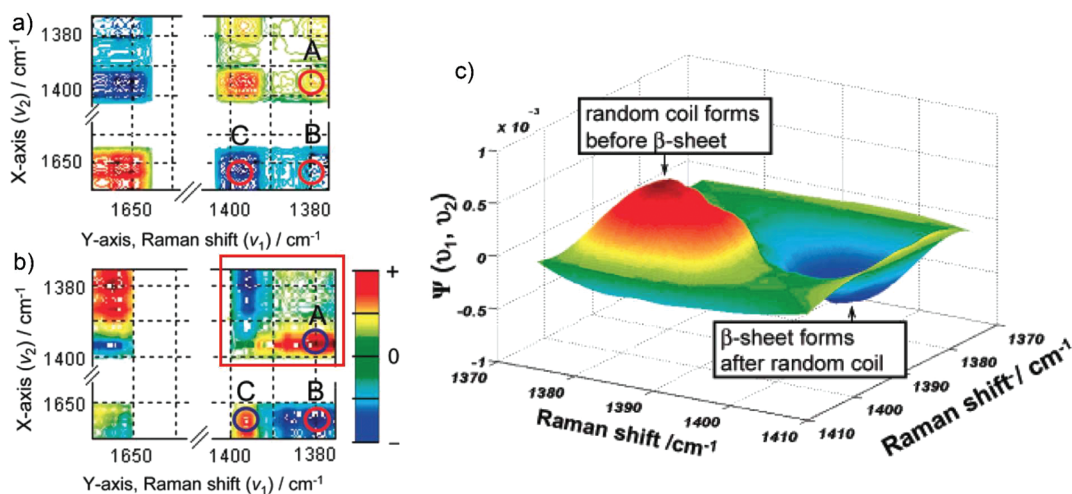
Figure 18. 2D correlation spectroscopy was used to establish sequential order of events during the fibrillation of hen egg white lysozyme. The synchronous (a) and asynchronous (b) 2D-DUVRR correlation maps of the $C_{\alpha}-$H bending region and α-helix sub-band of the Amide I region suggest the order of structural change to be random coil→ α-helix → β-sheet. Adapted with permission from ref 125. Copyright 1998. The 3D perspective plot (c) of the asynchronous $C_{\alpha}-$H bending region (red rectangle in (b)) illustrates the implication that random coil forms before β-sheet. (a and b) Adapted with permission from ref 137. Copyright 2008 American Chemical Society. (c) Adapted with permission from ref 136. Copyright 2007 American Chemical Society.

proteins and peptides fibrillize suggests that this conformation lies in the structural repertoire of proteins, in general. The association of fibrillation with human disease motivates investigations of the structure of these fibers and their mechanism of formation.[132] Unfortunately, the two classic tools of structural biology, X-ray crystallography and conventional NMR, are ill-suited for studying noncrystalline and insoluble full-length fibrils.[133] As shown below, deep UVRR is uniquely able to probe protein structure at all phases of fibrillation.[132−142] The use of chemometrics[143−150] and two-dimensional correlation spectroscopy (2DCoS) to these UVRR studies dramatically increases the information content, as shown below.

4.1. Two-Dimensional Correlation Deep UV Resonance Raman Spectroscopy

Two-dimensional correlation spectroscopy (2DCoS) has recently found increasing use in vibrational spectroscopy.[151] Vibrational 2DCoS is particularly beneficial for protein studies because it can resolve the often heavily overlapped bands in vibrational spectra into their separate components that arise from the various secondary structure motifs, amino acids, and side-chain groups. Additionally, the sequential temporal information regarding conformational changes provided by 2DCoS enables determination of structural transitions and kinetic reaction mechanisms.[137]

4.1.1. Fibril Nucleus Formation. Lednev's group demonstrated that deep UVRR combined with 2DCoS is a powerful tool for studying nucleus formation during fibrillation. Hen egg white lysozyme (HEWL), a protein chosen for its well-studied structural properties and folding/unfolding behaviors,[133] was used as a model for amyloidogenic proteins. Solutions of 70, 14, and 1.4 mg/mL of HEWL at pH 2.0 were incubated at 65 °C for various times. UVRR spectra were measured during incubation, and the resulting kinetic spectral data were analyzed using 2DCoS.[136]

Only random coil and β-sheet conformations are known to give rise to the $C_{\alpha}-$H bending region intensities observed in the $1380-1400$ cm^{-1} region. Lednev and co-workers correlated

$C_{\alpha}-$H region band intensities with other UVRR bands.[137] Synchronous $\Phi(\nu_1,\nu_2)$ and asynchronous $\Psi(\nu_1,\nu_2)$ 2D-Raman spectra were calculated using Noda's approach:

$$\Phi(\nu 1, \nu 2) + i\Psi(\nu 1, \nu 2) = \frac{1}{\pi(T_{\max} - T_{\min})}$$
$$\times \int_0^{\infty} \tilde{Y}_1(\omega)\tilde{Y}^*_2(\omega) \, d\omega \qquad (3)$$

where $\tilde{Y}_1(\omega)$ and $\tilde{Y}^*_2(\omega)$ are the forward and conjugate Fourier transforms, respectively, of the experimental spectral intensities $\tilde{y}(\nu,t)$ for all frequencies ν from ν_1 to ν_2, and incubation times t, during the observation period from $T_{\min}$ to $T_{\max}$.[136] In Figure 18, only the $C_{\alpha}-$H region and the α-helix sub-band of the Amide I region are shown for clarity.

The circled cross-peaks A, B, and C in Figure 18 represent the peaks relating β-sheet to disordered structure, α-helix to β-sheet, and α-helix to disordered structure, respectively. Because the synchronous cross-peak A is positive and cross-peaks B and C are negative, β-sheet and disordered structure are positively correlated. Conversely, the negative peaks B and C imply negative correlations between α-helix and β-sheet and between α-helix and disordered structure. The asynchronous 2D-Raman correlation map (Figure 18b) shows a positive peak at A, suggesting that a change in the disordered structure spectral region happens first. Considering the negative synchronous peak, and the negative asynchronous peak at B, it can be deduced that spectral changes in the disordered structure spectral region happen before changes in the α-helix region. Similarly, the negative synchronous peak, and the positive asynchronous peak at C implies that β-sheet spectral changes occur after α-helix changes.[137]

4.1.2. Apparent Inverse Order. It is notable that, at first glance, this interpretation of the 2D correlation maps suggests an anomalous sequence of events. Logically, α-helix melting needs to occur before any disordered structure can form. This apparent paradox is resolved by noting that the asynchronous 2DCoS probes both the sequential order of events in a chemical reaction

Table 1. Identifying the Possible Types of One- Or Two-Step Reaction Mechanisms Based on the Intensities of Synchronous and Asynchronous 2D Correlation Maps (Adapted with Permission from Ref 137; Copyright 2008 American Chemical Society)

observation		
intensities on synchronous map	intensities on asynchronous map[a]	possible mechanism
A and B negatively correlated	A and B are synchronous	A → B or A ⟷ B
A and B are negatively correlated at all stages of the reaction	B changes before A	A → B ⟷ P or A ⟷ B ⟷ P
correlation of A and B changes sign over the course of the reaction[b]	sequential order A → P → B or B → A → P	A → B → P or A ⟷ B → P

[a] Sequential order may change when varying the ratios of rate constants. Simulations using anticipated rate constants are advised when testing for all mechanisms. [b] This can also be the case for the reaction A ⟷ B ⟷ P and A → B ⟷ P.

and the average rate of concentration change of each species.[137] The latter is an important fact that, if overlooked, can lead to serious misinterpretation of spectroscopic data. This phenomenon can readily be explained by considering what contributes to an asynchronous 2D map. In any chemical reaction with the formation of an intermediate, the formation of the product will be in-phase with the decrease in the reactant, and thus, the intermediate should change slightly ahead to compensate for the delay in product formation.[137]

4.1.3. Extraction of Characteristic Times for Structural Changes. The characteristic times for the evolution of secondary and tertiary structures were extracted from the 2D-UVRR data by means of kv correlation analysis. Following the approach of Shanmukh and Dluhy,[152] the asynchronous correlation of the experimental decaying intensities with a reference set of exponentially decaying intensities was calculated by

$$\Psi(\tau, v) = \frac{1}{N-1} \sum_{j=0}^{N-1} y(v, n_j) \sum_{k=0}^{N-1} N_{jk} \times \exp\left(\frac{-t}{\tau} + R\right)$$

(4)

where $\Psi(\tau, v)$ is the correlation intensity at a point (τ, v); N is the total number of spectra; n_j is the order number of the spectrum; τ is the characteristic time of the exponential decay; N_{jk} is the Hilbert−Noda transformation matrix; R is the constant matrix; and $y(v, n)$ are the spectral intensities. After performing this analysis, the characteristic times were determined to be as follows: disordered structure formation ($\tau \approx 22$ h), tertiary structure and α-helix melting ($\tau \approx 30$ h), and nucleus β-sheet formation ($\tau \approx 35$ h).[137]

4.2. Elucidating the Kinetic Mechanism of Early Events of HEWL Fibrillation

The asynchronous 2D-Raman correlation map suggests that the mechanism is stepwise, rather than parallel; otherwise, the formation of random coil and β-sheet would be completely correlated.[136] This implies that one of the four possible two-step mechanisms below is occurring. Table 1 summarizes the possible observations and corresponding interpretations of the 2D correlation data.

mechanism 1: A → B → P
mechanism 2: A ⟷ B → P
mechanism 3: A→B ⟷ P
mechanism 4: A ⟷ B ⟷ P

It has been shown that the formation of a partially unfolded intermediate from native HEWL is an irreversible transition.[153] This eliminates mechanisms 2 and 4 as possibilities. An irreversible conversion of B to P (mechanisms 1 and 2) would appear in the 2D-Raman correlation map as a negative correlation

Table 2. Characteristic Times for Transformations of Native Lysozyme to Partially Unfolded Intermediate (τ_1), Partially Unfolded Intermediate to Nucleus (τ_2), and Nucleus to Partially Unfolded Intermediate (τ_{-2}) for Three Concentrations (Adapted with Permission from Ref 136; Copyright 2007 American Chemical Society)

	characteristic time, h		
concentration mg/mL	τ_1	τ_2	τ_{-2}
70	30 ± 2	70 ± 20	15 ± 5
14	30 ± 2	70 ± 10	12 ± 3
1.4	30 ± 2	74 ± 16	14 ± 5

between A and B at the beginning of the reaction, followed by a positive correlation between A and B for the remainder of the reaction. However, a reversible transition from B to P (mechanisms 3 and 4) would lead to a negative correlation between A and B at all stages of the reaction, which was the case for HEWL. Considering these details, only mechanism 3 remains, suggesting that the actual reaction mechanism is

$$\alpha\text{-helix} \xrightarrow{k_1} \text{disordered structure} \xrightleftharpoons[k_{-2}]{k_2} \beta\text{-sheet} \qquad (\text{model1})$$

The rate constants k_1, k_2, and k_{-2} were determined by using the experimentally determined[136] characteristic times (summarized in Table 2) for the following mechanism:

$$\text{native} \xrightarrow{K_1} \text{PU} \xrightleftharpoons[k_{-2}]{k_2} \text{nucleus} \qquad (\text{model2})$$

Relating the integrated rate laws for these two mechanisms yielded the following relations between the rate constants k_1, k_2, and k_{-2} and K_1, K_2, and K_{-2}:

$$\begin{aligned} k_1 &= K_1 \\ k_2 &= \frac{K_2}{1-R} \\ k_{-2} &= K_{-2} - \frac{R}{1-R} \times K_2 \end{aligned} \qquad (5)$$

where R is the fraction of disorded structure in native HEWL (60%[154] in this case). Taking K_i to be the reciprocal of the characteristic time τ_{K_i}, one obtains $K_1 = 0.033$ h^{-1}, $K_2 = 0.0125$ h^{-1}, $K_{-2} = 0.067$ h^{-1}, and thus, τ_{k_1}, τ_{k_2}, and $\tau_{k_{-2}}$ are 30, 32, and 21 h, respectively.[137]

A simulation-aided approach was utilized for model testing, and the results proved to be in close agreement with

2617

dx.doi.org/10.1021/cr200198a | Chem. Rev. 2012, 112, 2604−2628

experimental results. The rate constants k_1, k_2, and k_{-2} of model 1 were extracted by simulating different sets of rate constants k_i to calculate the evolution profiles of pure secondary structure. Using spectral profiles of the pure secondary structures, modeled as mixed Gaussian−Lorentzian shapes, and the simulated evolution profiles, kv correlation maps were constructed as described above and compared to the experimental kv correlation maps. When the characteristic times were extracted from the best-matched kv correlation map, as described above, and converted to rate constants K_i, the results were identical to the experimentally derived rate constants.[137]

These data are consistent with the step-by-step mechanism proposed by Dobson and co-workers:[155]

$$\text{Native} \rightarrow PU \Longleftrightarrow \beta\text{-sheet}$$

Seeding experiments were performed to further test this interpretation. The supernatant of a HEWL sample that had been incubated for 48 h was used to seed the fibrillation of fresh HEWL. The effective elimination of the fibrillation lag-phase observed is in complete agreement with the proposed mechanism.[136]

4.3. Structural Characterization of Fibrillar Proteins

4.3.1. Hydrogen−Deuterium Exchange.
Lednev and co-authors have combined hydrogen−deuterium exchange (HX) with UVRR to probe the secondary structure of the fibril cross-β core. HX is such a useful technique for characterizing protein structure because, in an amino acid residue, only the main chain NH group and O, N, and S bound protons can be exchanged easily, while the carbon-bound protons generally do not exchange.[156] This, combined with the fact that strongly hydrogen-bonded secondary structures greatly reduce the rate of hydrogen−deuterium exchange,[157] allows for a particularly clever use of HX to probe the fibril core. It was hypothesized that the tightly packed hydrophobic core of amyloid fibrils would experience a drastically reduced HX rate compared to the amide N−H protons in the unordered fragments (Figure 19).[140] Mikhonin and Asher have shown[87] that HX will cause a downshift of the amide II deep UVRR band from $\sim$1555 to $\sim$1450 cm^{-1} (amide II′) along with the virtual disappearance of the amide III band in an unordered protein.[142] Figure 20 illustrates these spectral changes in deep UVRR spectra of fibrillar and unordered lysozyme upon deuteration.

4.3.2. Bayesian Source Separation.
To deduce structural information about the fibril core, the overlapping spectral bands of the deuterated unordered fractions and the still-protonated cross-β core need to be resolved. The Bayesian approach[158] was utilized, instead of a blind source separation algorithm such as ICA or pure variable methods, because it is uniquely suited to solve extremely ill-suited MCR and prior-dominated problems.

4.3.3. Structure Determination of the Lysozyme Fibril Core.
Lednev and co-workers combined deep UVRR spectroscopy and hydrogen−deuterium exchange to probe the structure of HEWL fibrils.[142] The Bayesian signal dictionary approach was used to incorporate a priori information about characteristic spectral bands. In this work, the reference band library contained mixed Gaussian and Lorentzian shapes of certain widths and spectral positions obtained by fitting the deep UVRR spectra of fibrils with Gaussian/Lorentzian peaks having a
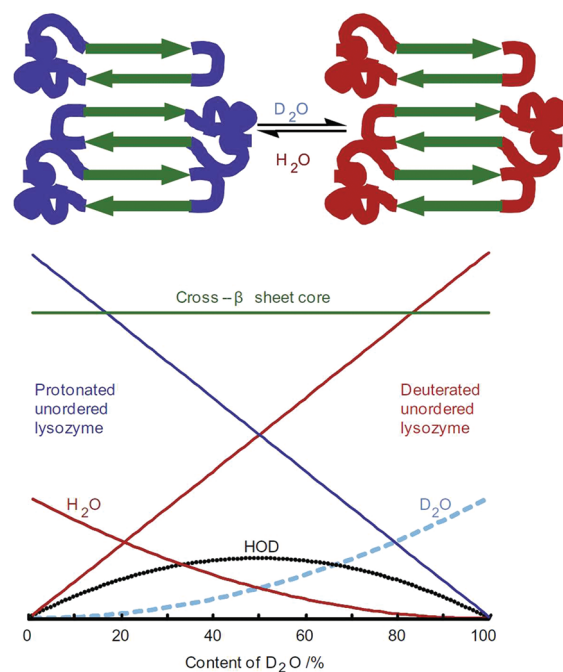

Figure 19. Hydrogen−deuterium exchange (HX) was used to allow for the extraction of the Raman signature of the fibril core. (Top) Schematic representation of HX: the protonated fibril core is protected from HX, while the unordered fraction is not. (Bottom) Expected concentration profile of major components vs the fraction of D_2O: protonated unordered lysozyme (blue), cross-β-sheet core (green), deuterated unordered lysozyme (red), H_2O (brown solid), HOD (black solid), and D_2O (light blue dashed). Reprinted with permission from ref 140. Copyright 2010 Elsevier.

predefined width range. Prior information regarding the experimental spectra of deuterated lysozyme and reference spectrum for the cross-β-sheet were incorporated by augmenting the matrices with an additional row. The final step is accomplished by using the floating-point genetic algorithm to determine the remaining parameters.[140]

By extracting the deep UVRR spectrum of the fibril core, the exact position of the amide III$_3$ (β) band could be determined, and the Asher group's method was used to calculate of the Ψ dihedral angle distribution.[142] The spectrum of the cross-β-core of HEWL fibrils extracted by this method is shown in Figure 21. The distribution of the Ψ dihedral angle obtained from the Raman signature of the fibril core provides an important characteristic of the polypeptide conformation and should allow for differentiating different types of crossβ-cores core in amyloid fibrils.

4.3.4. Structural Variations in the Cross-β Core.
4.3.4.1. YEHK Genetically Engineered Polypeptides. Over 20 structurally and functionally unrelated proteins that are associated with various neurodegenerative diseases form similar fibrillar assemblies despite the fact that the fibrillation conditions and the apparent mechanism of fibrillation are protein-specific. Lednev and co-workers utilized relatively simple polypeptides to mimic the fibril formation of globular proteins. Several synthetic polypeptides exhibiting typical fibrillogenic properties have been designed and synthesized by using genetic engineering.[159−162] These large polypeptides are soluble under close to physiological conditions but form fibrils under

2618

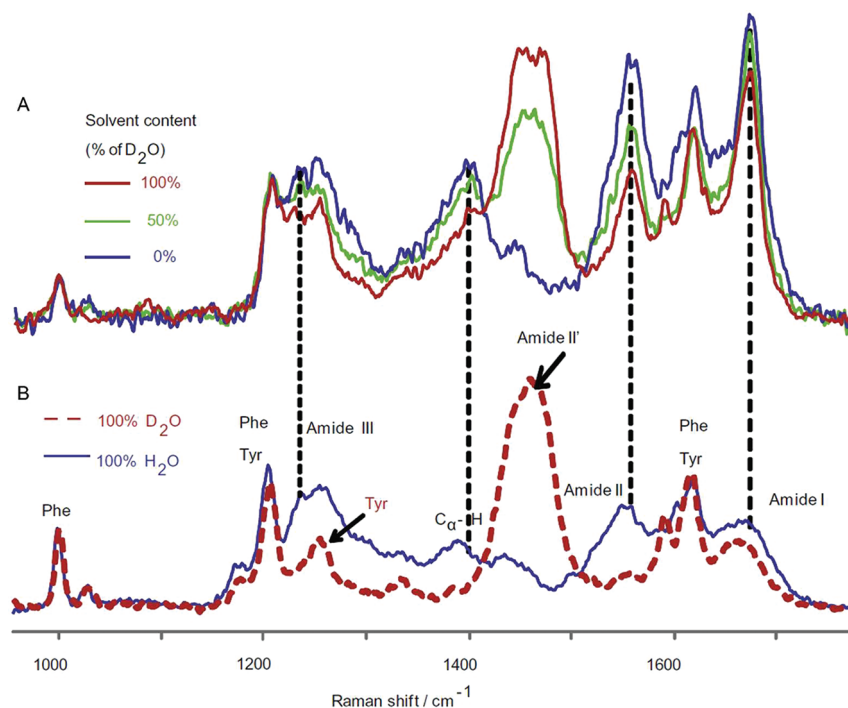dx.doi.org/10.1021/cr200198a |*Chem. Rev.* 2012, 112, 2604−2628

Figure 20. Deep UVRR spectral changes in fibrillar and unordered hen egg white lysozyme after hydrogen—deuterium exchange provide evidence of a still-protonated core. (A) DUVRR spectra of HEWL fibrils in H_2O (blue), D_2O (red), and 50/50% H_2O/D_2O mixture (green). (B) DUVRR spectrum of unordered lysozyme in H_2O (blue) and D_2O (red). Reprinted with permission from ref 140. Copyright 2010 Elsevier.
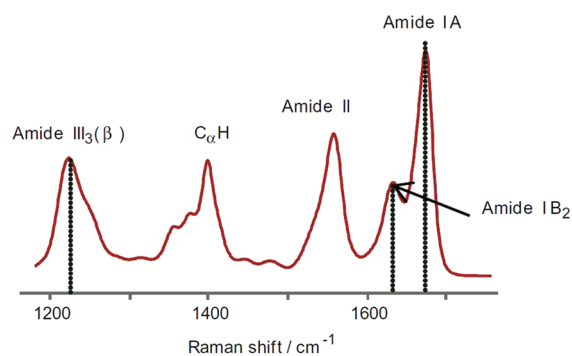

Figure 21. Deep UVRR spectrum of the cross-β-core of hen egg white lysozyme extracted using Bayesian source separation. Reprinted with permission from ref 140. Copyright 2010 Elsevier.
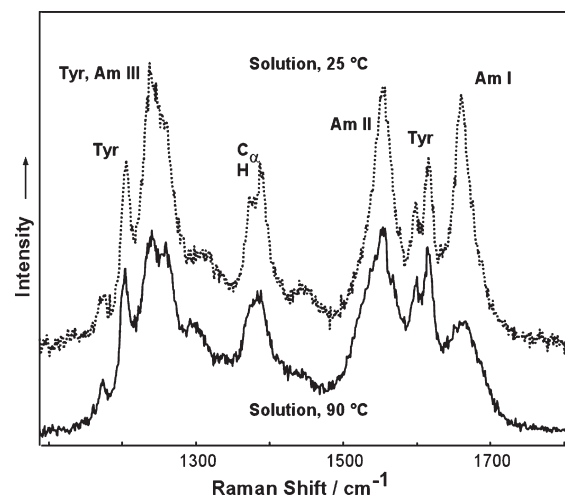

Figure 22. Deep UVRR spectra of a genetically engineered polypeptide (YEHK21) heated to various temperatures were recorded to detect spectral changes resulting from β-sheet melting. Deep UVRR spectra of YEHK21 in solution at 25 and 90 °C, illustrating spectral differences characteristic of β-sheet melting. Reprinted with permission from ref 163. Copyright 2006 Elsevier.

acidic pH. They exhibit a lag phase and show accelerated fibrillation on seeding or agitation. Genetic engineering allows for varying the polypeptide sequence to probe the sequence specific mechanism of fibrillation.

A large 687-residue polypeptide consisting of 32 amino acid repeats, $GH_6[(GA)_3GY(GA)_3GE(GA)_3GH(GA)_3GK]_{21}GAH_6$ (YEHK21), was found to form fibrils at room temperature.[163] The formation of these fibrils was thermoreversible. Deep UVRR spectra were recorded at various temperatures ranging from 25 to 90 °C, after reaching equilibrium. The most significant spectral changes occurred at temperatures greater than 80 °C. Figure 22 shows the Raman spectra of YEHK21 in solution measured at 25 and 90 °C. The spectra demonstrate changes consistent with the melting of a β-sheet structure into an unordered conformation. Spectra measured at various

times after heating were virtually the same, indicating a slow recovery process.[163]

The analysis of polypeptide secondary structure content was complicated by the temperature dependence of the basis spectra. This was overcome by exploiting the slow recovery process. Deep UVRR spectra were recorded after 5 min of heating to various temperatures ranging from 25 to 125 °C and subsequent rapid cooling to room temperature.
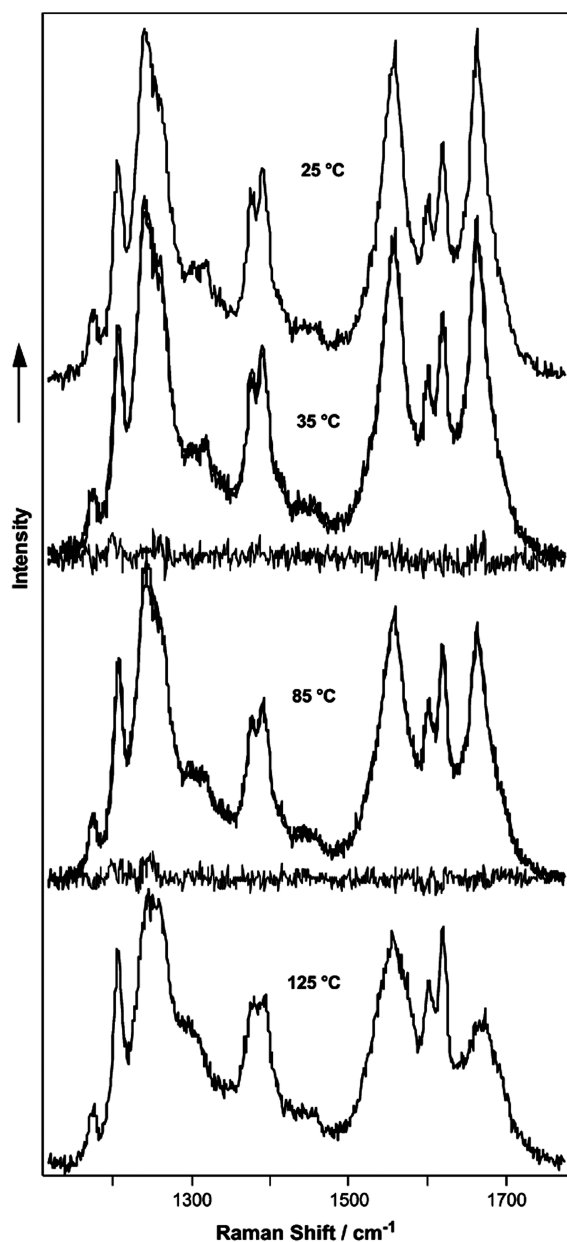
Figure 23. Because of the temperature dependence of the basis spectra, all measurements had to be recorded at the same temperature to allow for evaluation of conformational changes of the YEHK21 polypeptide. The experimental spectra were fit using basis spectra of completely folded and unordered YEHK21, and tyrosine. Deep UVRR spectra of YEHK21 measured at room temperature after 5 min of heating to 35, 85, and 125 °C. Calculated spectra and difference spectra between the measured and calculated ones are shown for 35 and 85 °C. Reprinted with permission from ref 163. Copyright 2006 Elsevier.

In this way, all measurements were taken at the same temperature, ensuring any spectral changes were a result of temperature-induced conformational changes (Figure 23). This spectral data set was used for understanding YEHK21 polypeptide melting.[163]

A melting curve was constructed using a basis set of three deep UVRR spectra: the YEHK21 backbone Raman spectra (initial sample and sample treated at 125 °C) and the deep UVRR
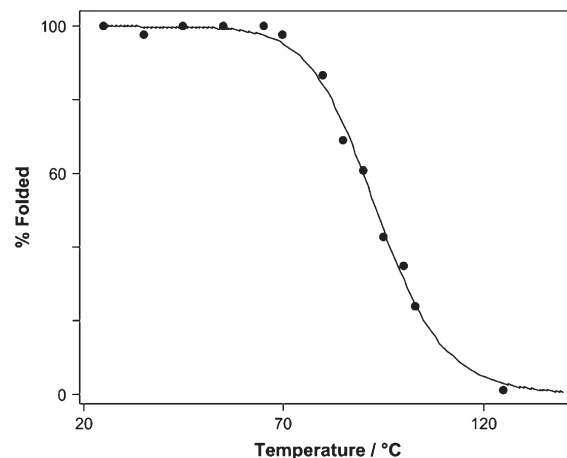

Figure 24. YEHK21 melting curve was constructed by plotting the fraction of folded peptide against temperature (solid circles). The solid line represents the best fit for eq 6. Reprinted with permission from ref 163. Copyright 2006 Elsevier.

spectrum of tyrosine. The first two spectra represent completely folded YEHK21 (mostly β-sheet and turn conformations) and the unordered YEHK21 (mainly polyproline II conformation), while tyrosine was included for use as an internal standard. These three basis spectra were used to fit the Raman spectra of YEHK21 at various temperatures; Figure 23 shows the calculated and residual spectra for the samples treated at 35 and 85 °C. This showed that the melting process could be considered as a two-state process with each spectrum described with different proportions of β-sheet and turn/polyproline II conformations. The percent of folded contribution was plotted versus temperature to create the melting curve of Figure 24.[163]

Thermodynamic parameters were estimated by fitting the data to

$$f_F = \frac{1}{1 + e^{-\left(\frac{\Delta H}{RT} - \frac{\Delta S}{R}\right)}} \tag{6}$$

where f_F is the fraction of folded polypeptide after treatment at temperature T and R is the gas constant. The parameters ΔH and ΔS were determined to be 135 ± 14 kJ/mol and 370 ± 40 J/(mol K), where the standard error was represented by ±2σ. This represents a first approximation because eq 6 is typically applied to two-state processes where ΔC_p, the heat capacity change, has negligible effect on the enthalpy of folding over the narrow temperature range of the transition.[164]

Temperature dependent measurements were performed to analyze the slow kinetics of YEKH21 β-sheet melting. The deep UVRR spectra of YEHK21 were collected every 20 s after a temperature jump from 25 to 85 °C (Figure 25a). The results of the temperature-jump experiments were similar to the steady-state measurements; the spectrum in Figure 25d is quite similar to those shown in parts b, c, e, and f of Figure 25. It was also found that recovery of the YEHK21 Raman spectrum was dependent on the temperature to which it was heated before being cooled to room temperature. Complete recovery of the YEHK21 Raman spectrum was observed after ~6 h of standing at room
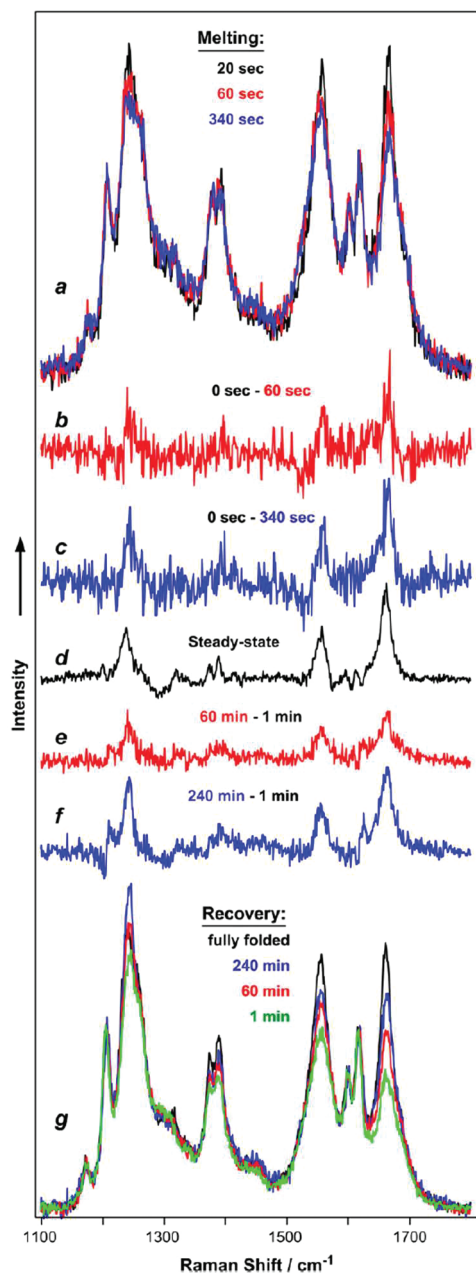
Figure 25. Temperature dependent measurements were made to assess the kinetics of β-sheet melting, the results of which were quite close to those observed in steady-state measurements. A temperature dependence of the extent of recovery of the starting deep UVRR spectrum was also observed. Deep UVRR spectra of YEHK21 measured at 20, 60, and 340 s after temperature jump (a). Difference spectra of deep UVRR spectrum measured before and 60 s (b) and 340 s (c) after temperature jump. Difference spectrum of deep UVRR spectra of initial folded YEHK21 and that measured at room temperature after being briefly heated to 125 °C (d). Difference spectrum of deep UVRR spectra of initial folded YEHK21 subtracted from that measured at room temperature 60 min (e) and 240 min (f) after being briefly heated to 100 °C. Deep UVRR spectra measured at room temperature 1, 60, and 240 min after a 5 min heating to 100 °C (g). Reprinted with permission from ref 163. Copyright 2006 Elsevier.

temperature after being briefly heated to 85 °C. On the other hand, only 80% recovery was achieved after a 5 min heating to

100 °C before sitting at room temperature for 4 h. The kinetics for the recovery of the deep UVRR spectrum after heating was determined to be roughly monoexponential with a characteristic time of ~1 h.[163]

A study of three similarly engineered polypeptides that form amyloid-like fibrils provided the first direct evidence that the structure of the cross-β core is sequence-dependent. The three polypeptides consisted of seven repeats of 32, 40, or 48 amino acid repeats, $(GA)_nGY(GA)_nGE(GA)_nGH(GA)_nGK$ (n = 3, 4, or 5, respectively, 32YEHK7, 40YEHK7, or 48YEHK7). These β-sheet-forming repetitive polypeptide blocks and selected amino acids at turn positions facilitated the formation of the targeted amyloid-like fibrils[141] (Figure 26A). These polypeptides were designed to have the same turn structure so any pairwise subtraction would result in the pure resonance Raman spectra of the fibrillar β-sheet core.[140] The validity of this hypothesis is verified by inspecting the difference spectrum in Figure 26C, where they are virtually identical within experimental error.[141]

The studies above are the first direct measurements of the β-turn spectroscopic signature. Pure variable methods[165] (see Supporting Information) were used to analyze the spectra of the YEHK fibrils to resolve the contributions from the β-sheet and β-turn portions. The spectra of the two components were calculated and the experimental spectra of the YEHK fibrils were able to be fit with a linear combination of the two components (Figure 27). Using the Raman signature of the cross-β core, the dominant amide III peak was found to be at 1241 cm^{-1}, corresponding to a Ψ angle of 150° and an antiparallel β-sheet conformation. The narrow Ramachandran Ψ angular distribution of YEHK fibrils suggests a highly ordered β-sheet,[141] consistent with the findings reported on lysozyme fibrils.[142] Notably, however, the UVRR spectra of the cross-β core of YEHK and lysozyme were different, indicating a sequence dependence of the core β-structure.[141]

4.3.4.2. Amyloid β. The application of the HX-DUVRR method to amyloid-β (Aβ) fibrils revealed that parallel and antiparallel β-sheets have different distributions of Ψ dihedral angles. Full-length unlabeled Aβ_{1-40} peptide and Aβ_{32-42} fragment fibrils were subjected to post fibrillation HX, UVRR spectra of the fibrillar core were extracted, and the Ψ dihedral angle distributions were calculated. It was shown that Aβ_{1-40} peptide exhibited a parallel β-sheet conformation, atypical for globular proteins, and that Aβ_{32-42} fragment fibrils possessed the more typical antiparallel conformation.[135] The availability of the 3-dimensional structure of the Aβ_{1-40} fibrils obtained by solid-state NMR[166] was used to verify the applicability of the Asher group's approach[82] for the quantitative characterization of peptide conformation in the fibril core using DUVRR spectroscopy.

Using this structural information, the amide III region of the deep UVRR spectra of the Aβ_{1-40} fibril core was calculated by using the following method and compared to experimental results. The contributions of each peptide residue in the β-strand that was resistant to HX were calculated using a set of residue-specific Ψ angles reported for the Aβ_{1-40} fibril core[166] as Gaussian curves with a half-width at half-maximum of 13 cm^{-1}. As shown in Figure 28b, the calculated spectrum (blue) is in excellent agreement with the experimental spectrum (black). It is notable that there is a significant difference in the spectral profile of the Aβ_{1-40} fibril core (Figure 28b) and those of the Aβ_{32-42} (Figure 30a), hamster prion protein, and YEHK
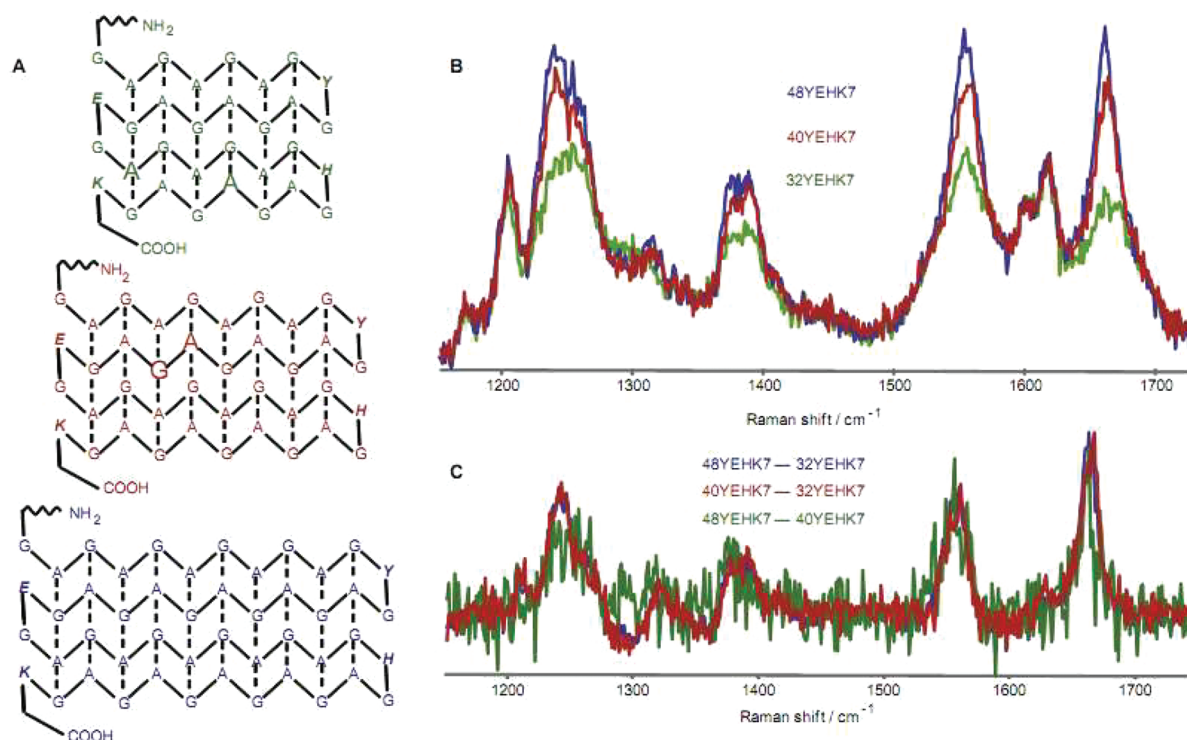
Figure 26. Three genetically engineered polypeptides with virtually identical turn contributions were used to establish the first direct measurement of the β-turn Raman signature. The similarities in the difference spectra confirm the validity of this approach. (A) Schematic representation of 32YEHK7, 40YEHK7, and 48 YEHK7 polypeptide amyloid fibril building blocks. (B) Deep UVRR spectra and (C) difference spectra of 32YEHK7, 40YEHK7, and 48 YEHK7. Adapted with permission from ref 140. Copyright 2010 Elsevier.
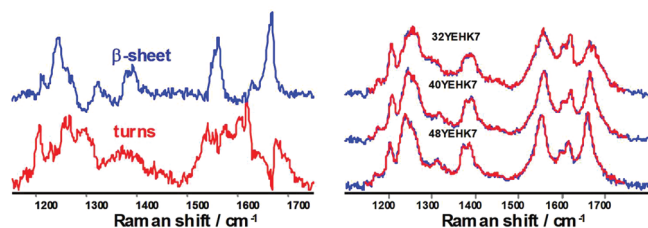
Figure 27. Deep UVRR spectral signatures of YEHK polypeptide β-sheet and turns fit the experimental spectra with close agreement, indicating that these peptides are composed primarily of these two structures. Deep UVRR spectra of β-sheet and turns (left), and the deep UVRR spectra of YEHK fibrils fitted with a linear combination of these two components (right). Adapted with permission from ref 141. Copyright 2008 American Chemical Society.

peptide (Figure 28c). The major difference between the calculated amide III band region and the experimentally measured one is the appearance of two bands at 1280 and 1250 cm^{-1}. These bands, however, are also present in the spectrum of Aβ_{32-42} and are outside the β-sheet region, indicating that these peaks are most likely not part of the amide III$_3$ vibration and do not interfere with the analysis.

4.3.5. Aromatic Side Chain as a Reporter of Local Environment. Xu et al.[133] assessed phenylalanine's ability to act as an intrinsic deep UVRR spectroscopic probe of local environment. A 1.17 mM N-acetyl-L-phenylalanine ethyl ester (ac-phe-ee) solution in acetonitrile was diluted in a series of acetonitrile−water solutions with a final acetonitrile content ranging from 5% to 100%, and deep UVRR spectra were

recorded. As seen in Figure 29, the spectra comprised two strong peaks corresponding to acetonitrile, and several prominent phenylalanine bands. The band at 1000 cm^{-1}, derived from phenyl ring stretching, exhibited the strongest change in Raman cross section as the concentration of acetonitrile varied. The inset of Figure 29 shows that the Raman cross section of this band increases monotonically, reaching a plateau at ∼50% acetonitrile. Practically, this indicates that the 1000 cm^{-1} band of phenylalanine is sensitive to water exposure, making it a probe of protein local environment and tertiary structure.

In the study of HEWL, deep UVRR spectra were recorded at various stages of fibrillation, analyzing the supernatant and gelatinous phase separately (Figure 30). The spectra were dominated by contributions of the amide chromophore and phenylalanine. There was a dramatic reduction in the 1000 cm^{-1} phenylalanine band intensity with increased incubation time. Figure 31 shows the monoexponential decrease with a characteristic time of 29 ± 2 h. This indicates that phenylalanine is increasingly exposed to water as fibrillation progresses.[137]

Wang and JiJi also used deep UVRR spectroscopy to study amyloid-β (Aβ) peptide fibrillation.[167] They observed that the intensities of phe and tyr bands increase upon addition of myricetin, which inhibits Aβ peptide fibrillation. They concluded that myricetin interacts with these aromatic amino acid side chains and prohibits fibrillation of Aβ peptide.

4.4. Spontaneous Refolding of Amyloid Fibrils from One Polymorph to Another

Amyloid fibrils prepared from full-length proteins are typically very stable and considered to be the most thermodynamically
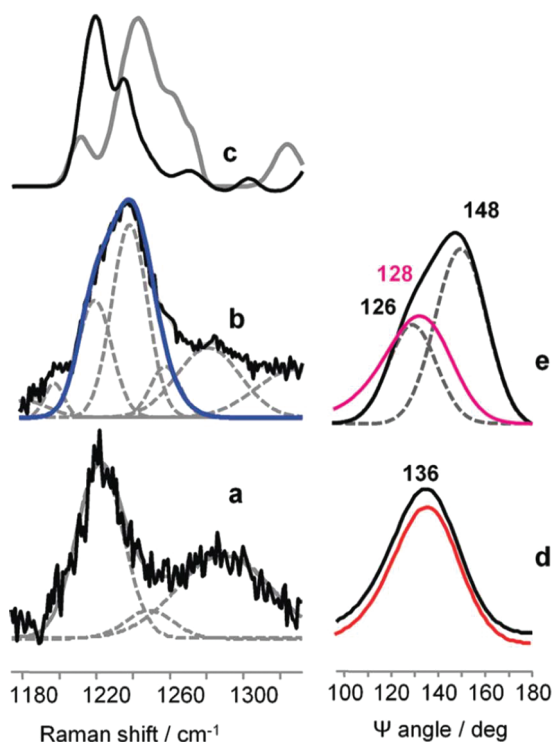
Figure 28. Solid-state NMR data of $A\beta_{1-40}$ fibrils were used to verify the applicability of the Asher group's Ψ distribution method to quantitatively characterize the fibril core conformation of peptides using deep UVRR spectroscopy. (a) Deep UVRR spectra of the $A\beta_{34-42}$ fibril core (solid line) and the best fit with Gaussian peaks (dotted lines); (b) deep UVRR spectra of the $A\beta_{1-40}$ fibril core (solid line) and the best fit with Gaussian peaks (dotted lines) and the calculated spectrum based on SSNMR data (blue line); (c) hamster prion protein (black) and YEHK peptide (gray); (d) Ψ angle distribution in the $A\beta_{34-42}$ fibril core (black) and average antiparallel β-sheets in globular proteins; (e) calculated Ψ angle distribution in the $A\beta_{1-40}$ fibril core (black), the best fit with Gaussian curves (dashed lines), and the Ψ angle distribution in average parallel β-sheets in globular proteins (pink). Adapted with permission from ref 135. Copyright 2010 American Chemical Society.

Figure 30. Deep UV resonance Raman spectra of hen egg white lysozyme were recorded at various times of incubation. Not incubated (A), soluble phase after 2 days of incubation (B), and the gelatinous phase (C). * is the internal standard peak. Reprinted with permission from ref 133. Copyright 2008.
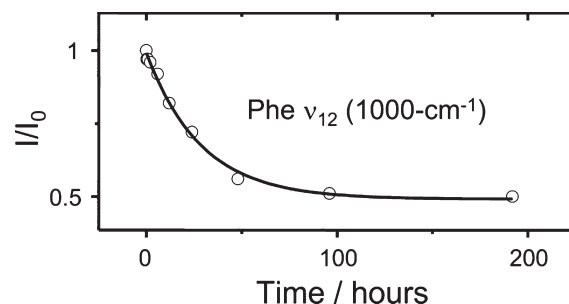
Figure 31. Local environment of hen egg white lysozyme was probed using phenylalanine as an intrinsic reporter. The relative intensities of the 1000 cm^{-1} band of phenylalanine from the Raman spectra of HEWL were plotted as a function of incubation time, indicating an increasing exposure of phenylalanine to water as fibrillation progresses. Reprinted with permission from ref 133. Copyright 2008.
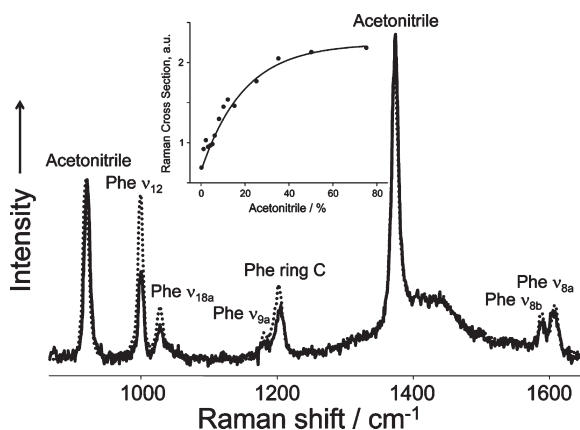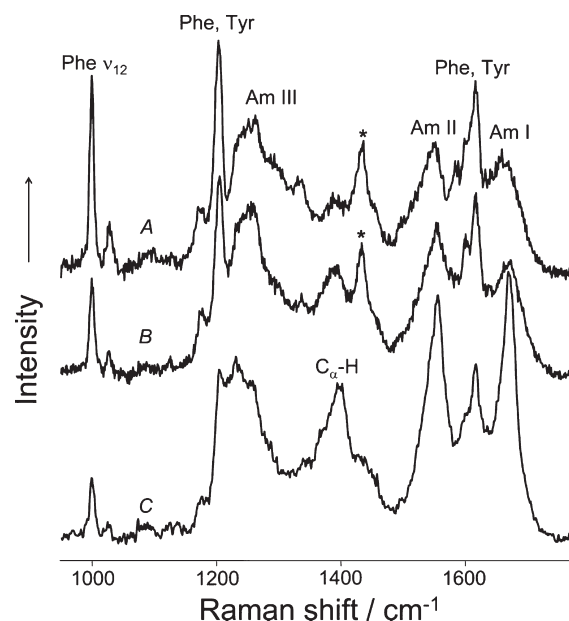

Figure 29. Raman cross section of the 1000 cm^{-1} phenylalanine band was shown to vary as a function of water exposure, making it a useful probe of local environment. Deep UV resonance Raman spectra of N-acetyl-L-phenylalanine ethyl ester in water and 50% acetonitrile (dotted line) and 5% acetonitrile (solid line). Inset: Raman cross section of the 1000 cm^{-1} band as a function of acetonitrile concentration. Reprinted with permission from ref 133. Copyright 2008.

stable form of proteins because of the high resistance to thermal and solvent-induced denaturation.[168,169] Very harsh denaturating conditions such as high pH, low temperature, and high pressure are required to disintegrate mature fibrils,[170,171] and no newly formed fibrils are expected to appear under such conditions. The ability of mature fibrils to change their structure and morphology has not been questioned, to the best of our knowledge, because no conventional methods would allow its detection without special sample preparation.

Kurouski et al.[172] utilized deep UVRR spectroscopy to monitor the stability of apo-α-lactalbumin fibrils during the preparation of samples for atomic force microscopic (AFM) characterization. UVRR spectroscopy was chosen because it does not require any sample preparation. Surprisingly, melting
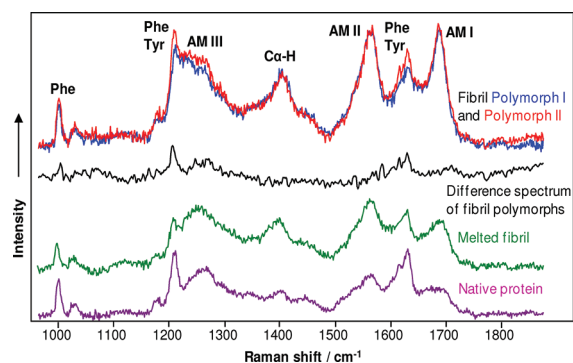
Figure 32. Spontaneous refolding of apo-α-lactalbumin fibrils from one polymorph to another after the temperature was dropped by 12 °C and the solution was desalted. DUVRR spectra of native apo-α-lactalbumin, fibril polymorph I (prepared at 37 °C), partially melted fibrils after 5 h of incubation at 25 °C, and fibril Polymorph II (after 8 h of incubation at 25 °C). Reprinted with permission from ref 172. Copyright 2010 Royal Society of Chemistry.

and refolding of β-sheet was evident in the Raman spectra measured for mature apo-α-lactalbumin fibrils after the temperature was dropped from 37 to 25 °C and the solution was desalted (Figure 32).

Later, deep UVRR spectroscopy was also used to characterize the initial (polymorph I) and final (polymorph II) polymorphs.[172] The hydrogen−deuterium exchange combined with deep UVRR spectroscopy (see above for details) indicated that the amide III$_3$ region of the polymorph I spectrum shows two strong peaks at 1226 and 1253 cm^{-1}, corresponding to Ψ dihedral angles of 134.5 and 163.5°, respectively. Polymorph II, however, only exhibited a peak at 1253 cm^{-1} suggesting only a single β-sheet form is present, clearly indicating a difference in the structure of the fibril cores.[134] This result showed that changes in the fibril cross-β core correlate with noticeable changes in fibril morphology, indicating that apo-α-lactalbumin fibril polymorphism is correlated by a specific organization of the fibril core. The application of deep UVRR spectroscopy provided a unique opportunity for detecting the spontaneous transition between the two fibril polymorphs, observations that were not easily evident by using other conventional biophysical methods.[172]

5. CONCLUSIONS

UVRR is a powerful tool for the study of biomolecular structure and dynamics. The field is at present small due to the costs of instrumentation and the lack of commercial instruments. The instrumentation will continue to advance due to improvements in laser technology and the development of UV Raman spectrometers with dramatically improved signal-to-noise ratio (SNR) that will enable secondary structure conformational analysis at the level of single peptide bonds in large proteins.

With sufficient SNR, the Gibbs free energy landscape of individual peptide bonds in a peptide or protein can be incisively measured by selective isotopic labeling of individual peptide bonds. The difference spectrum between the labeled and the natural abundance protein would reveal the AmIII$_3$ band of each peptide bond; the frequencies and bandshapes will reveal the distribution in Ψ angles for each peptide bond.

The resulting Gibbs free energy landscape for each isotopically substituted peptide bond will specify the individual peptide bond energy landscape. T-jump kinetic measurements can probe the activation barriers that control (un)folding mechanisms.

Deep UVRR is uniquely suitable for structural characterization of proteins at all stages of amyloid fibril formation. The combination of hydrogen−deuterium exchange with DUVRR spectroscopy allows for probing the variations in cross-β core structure of fibril polymorphs. The application of advanced statistics, chemometrics, and two-dimensional correlation spectroscopy in particular for DUVRR spectra analysis significantly increases the quality and amount of information on protein structure and dynamics. This approach is especially useful for establishing the kinetic mechanisms of amyloid fibrillation.

ASSOCIATED CONTENT

Ⓢ Supporting Information

Supporting Information includes information on chemometrics and SIMPLISIMA. This information is available free of charge via the Internet at http://pubs.acs.org/.

AUTHOR INFORMATION

Corresponding Author

*E-mail: asher@pitt.edu. Phone: 412-624-8570. Fax: 412-624-0588.

Present Addresses

§Canmet Energy Technology Centre, 1 Oil Patch Drive, Devon, Alberta, Canada T9G 1A8

BIOGRAPHIES

Sulayman Oladepo received his Ph.D. from the University of Alberta in 2010, under the supervision of Prof. Glen Loppnow. He spent a year as a postdoctoral associate in the laboratory of Prof. Sanford Asher at the University of Pittsburgh, where he used UV resonance Raman spectroscopy to study the melting dynamics of β-sheet structures and the effects of citrullination on protein folding dynamics. He is currently a visiting fellow at Canmet Energy Technology Centre, Devon, Alberta. His current research involves photoacoustic FTIR and Raman spectroscopic characterization of asphaltenes.

Kan Xiong received his Bachelor's Degree in Chemistry from the University of Science and Technology of China in 2006. He is currently a senior graduate student under the direction of Prof. Sanford A. Asher at the University of Pittsburgh and is working on using Raman spectroscopy to study peptide folding, peptide fibrillization and $Cl^- \rightarrow H_2O$ charge transfer.

Zhenmin Hong is currently a graduate student in the Department of Chemistry, University of Pittsburgh. He received B.S. and M.S. degrees from Tsinghua University, China. His research interest includes using UV resonance Raman spectroscopy to study protein and peptide structure and folding. He is now examining the effect of side-chain interactions on determining peptide conformations.

Sanford Asher is Distinguished Professor of Chemistry at the University of Pittsburgh. He received his Bachelor's degree from

the University of Missouri at St. Louis in 1971 and his Ph.D. in 1977 from UC Berkeley. Following postdoctoral work in Applied Physics at Harvard, he joined the department of Chemistry of the University of Pittsburgh in 1980. His current research concentrates on developing UV resonance Raman spectroscopy for probing protein structure and dynamics. His research group also investigates and develops photonic crystal materials and sensors.

Joseph Handen received his Bachelor's Degree in Chemistry from the University at Albany, State University of New York, in 2009. He is currently a graduate student in Dr. Igor Lednev's research group at the University at Albany, State University of New York, and is working on using Raman spectroscopy to study β-sheet structures in amyloidogenic polypeptides.

Igor K. Lednev is an associate professor at the University at Albany, State University of New York. He graduated from the Moscow Institute of Physics and Technology, Russian Federation, receiving his Ph.D. degree in 1983. Then Dr. Lednev worked at the Institute of Chemical Physics, Russian Academy of Sciences, as a group leader. He joined the University at Albany in 2002. Dr. Lednev's research is focused on the development and application of novel laser spectroscopy for biomedical research and forensic purposes.

ACKNOWLEDGMENT

REFERENCES

(1) Baldwin, R. L.; Rose, G. D. *Trends Biochem. Sci.* **1999**, *24*, 26.
(2) Baldwin, R. L.; Rose, G. D. *Trends Biochem. Sci.* **1999**, *24*, 77.

(3) Dobson, C. M. *Philos. Trans. R. Soc., B* **2001**, *356*, 133.

(4) Dobson, C. M.; Sali, A.; Karplus, M. *Angew. Chem., Int. Ed.* **1998**, *37*, 868.

(5) Jahn, T. R.; Radford, S. E. *FEBS J.* **2005**, *272*, 5962.

(6) Lindberg, M. O.; Oliveberg, M. *Curr. Opin. Struct. Biol.* **2007**, *17*, 21.

(7) Daggett, V.; Fersht, A. *Nat. Rev. Mol. Cell Biol.* **2003**, *4*, 497.

(8) Anfinsen, C. B.; Haber, E.; Sela, M.; White, F. H., Jr. *Proc. Natl. Acad. Sci. U. S. A.* **1961**, *47*, 1309.

(9) Matthews, C. R. *Annu. Rev. Biochem.* **1993**, *62*, 653.

(10) Thirumalai, D.; Woodson, S. A. *Acc. Chem. Res.* **1996**, *29*, 433.

(11) Kim, P. S.; Baldwin, R. L. *Annu. Rev. Biochem.* **1982**, *51*, 459.

(12) Karplus, M.; Weaver, D. L. *Nature* **1976**, *260*, 404.

(13) Baldwin, R. L. *Trends Biochem. Sci.* **1989**, *14*, 291.

(14) Daggett, V.; Fersht, A. R. *Trends Biochem. Sci.* **2003**, *28*, 18.

(15) Dill, K. A.; Ozkan, S. B.; Shell, M. S.; Weikl, T. R. *Annu. Rev. Biophys.* **2008**, *37*, 289.

(16) Dill, K. A.; Chan, H. S. *Nat. Struct. Biol.* **1997**, *4*, 10.

(17) Dill, K. A. *Protein Sci.* **1999**, *8*, 1166.

(18) Zhuravlev, P. I.; Papoian, G. A. *Q. Rev. Biophys.* **2010**, *43*, 295.

(19) Kim, J.; Keyes, T.; Straub, J. E. *Phys. Rev. E: Stat., Nonlinear, Soft Matter Phys.* **2009**, *79*, 030902.

(20) Rylance, G. J.; Johnston, R. L.; Matsunaga, Y.; Li, C. B.; Baba, A.; Komatsuzaki, T. *Proc. Natl. Acad. Sci. U. S. A.* **2006**, *103*, 18551.

(21) Angelani, L.; Ruocco, G. *EPL* **2009**, *87*, 18002.

(22) Zhuravlev, P. I.; Papoian, G. A. *Curr. Opin. Struct. Biol.* **2010**, *20*, 16.

(23) Oliveira, L. C.; Schug, A.; Onuchic, J. N. *J. Phys. Chem. B* **2008**, *112*, 6131.

(24) Gruebele, M. *Proc. Natl. Acad. Sci. U. S. A.* **2009**, *106*, 18879.

(25) Mello, C. C.; Barrick, D. *Proc. Natl. Acad. Sci. U. S. A.* **2004**, *101*, 14102.

(26) Levy, Y.; Jortner, J.; Becker, O. M. *Proc. Natl. Acad. Sci. U. S. A.* **2001**, *98*, 2188.

(27) Karplus, M.; McCammon, J. A. *Nat. Struct. Biol.* **2002**, *9*, 646.

(28) Noé, F.; Schütte, C.; Vanden-Eijnden, E.; Reich, L.; Weikl, T. R. *Proc. Natl. Acad. Sci. U. S. A.* **2009**, *106*, 19011.

(29) Freddolino, P. L.; Harrison, C. B.; Liu, Y.; Schulten, K. *Nat. Phys.* **2010**, *6*, 751.

(30) Cantor, C. R.; Schimmel, P. R. In *Biophyical Chemistry*; McCombs, L. W., Ed.; W. H. Freeman and Company: San Francisco, 1980; Vol. 2; p 402.

(31) Rosenheck, K. D., P. *Proc. Natl. Acad. Sci. U. S. A.* **1961**, *47*, 1775.

(32) Saxena, V. P.; Wetlaufer, D. B. *Proc. Natl. Acad. Sci. U. S. A.* **1971**, *68*, 969.

(33) Greenfield, N. J.; Fasman, G. D. *Biochemistry* **1969**, *8*, 4108.

(34) Dickerson, R. E. *Annu. Rev. Biochem.* **1972**, *41*, 815.

(35) Strandberg, B.; Dickerson, R. E.; Rossmann, M. G. *J. Mol. Biol.* **2009**, *392*, 2.

(36) Moffat, K. *Acta Crystallogr., Sect. A* **1998**, *54*, 833.

(37) Mittermaier, A.; Kay, L. E. *Science* **2006**, *312*, 224.

(38) Billeter, M. *Q. Rev. Biophys.* **1992**, *25*, 325.

(39) Wuthrich, K. *Acta Crystallogr., Sect. D: Biol. Crystallogr.* **1995**, *51*, 249.

(40) Frank, A. T.; Stelzer, A. C.; Al-Hashimi, H. M.; Andricioaei, I. *Nucleic Acids Res.* **2009**, *37*, 3670.

(41) Andronesi, O. C.; Becker, S.; Seidel, K.; Heise, H.; Young, H. S.; Baldus, M. *J. Am. Chem. Soc.* **2005**, *127*, 12965.

(42) Williams, S.; Causgrove, T. P.; Gilmanshin, R.; Fang, K. S.; Callender, R. H.; Woodruff, W. H.; Dyer, R. B. *Biochemistry* **1996**, *35*, 691.

(43) Hendra, P. J. In *Handbook of vibrational spectroscopy*; Chalmers, J. P., Griffiths, P. R., Eds.; John Wiley & Sons: London, 2002; Vol. 2.

(44) Everall, N. In *Handbook of vibrational spectroscopy*; Chalmers, J. P., Griffiths, P. R., Eds.; John Wiley & Sons: London, 2002; Vol. 1.

(45) Weber, A. In *Handbook of vibrational spectroscopy*; Chalmers, J. P., Griffiths, P. R., Eds.; John Wiley & Sons: London, 2002; Vol. 1.

(46) Long, D. A. *The Raman Effect: A unified treatment of the theory of raman scattering by molecules*; West Sussex, England, 2002.

(47) Kramers, H.; Heisenberg, W. *Z. Phys. A* **1925**, *31*, 681.

(48) Dirac, P. A. M. *Proc. R. Soc. A* **1927**, *114*, 710.

(49) Placzek, G. In *Handbuch der Radiologie*; Marx, E., Ed.; Aeademische: Leipzig, Germany, 1934; Vol. 6.

(50) Albrecht, A. C. *J. Chem. Phys.* **1961**, *34*, 1476.

(51) Lee, S.-Y.; Heller, E. J. *J. Chem. Phys.* **1979**, *71*, 4777.

(52) Tannor, D. J.; Heller, E. J. *J. Chem. Phys.* **1982**, *77*, 202.

(53) Heller, E. J.; Sundberg, R.; Tannor, D. *J. Phys. Chem.* **1982**, *86*, 1822.

(54) Asher, S. A. *Annu. Rev. Phys. Chem.* **1988**, *39*, 537.

(55) Myers, A. B. *J. Raman Spectrosc.* **1997**, *28*, 389.

(56) Asher, S. A. *Anal. Chem.* **1993**, *65*, A59.

(57) Asher, S. A. *Anal. Chem.* **1993**, *65*, A201.

(58) Palaniappan, V.; Bocian, D. F. *Biochemistry* **1994**, *33*, 14264.

(59) Chi, Z. H.; Asher, S. A. *Biochemistry* **1998**, *37*, 2865.

(60) Balakrishnan, G.; Hu, Y.; Oyerinde, O. F.; Su, J. T.; Spiro, T. G. *J. Am. Chem. Soc.* **2007**, *129*, 504.

(61) Ray, G. B.; Copeland, R. A.; Lee, C. P.; Spiro, T. G. *Biochemistry* **1990**, *29*, 3208.

(62) Ahmed, Z.; Beta, I. A.; Mikhonin, A. V.; Asher, S. A. *J. Am. Chem. Soc.* **2005**, *127*, 10943.

(63) Asher, S.; Johnson, C. *Science* **1984**, *225*, 311.

(64) Terner, J. S., J. D.; Spiro, T. G.; Nagumo, M.; Nicol, M.; El-Sayed, M. A. *Proc. Natl. Acad. Sci. U. S. A.* **1981**, *78*, 1313.

(65) Smulevich, G.; Spiro, T. G. *Biochim. Biophys. Acta* **1985**, *830*, 80.

(66) Asher, S. A.; Johnson., C. R.; Murtaugh, J. *Rev. Sci. Instrum.* **1983**, *54*, 1657.

(67) Bykov, S.; Lednev, I.; Ianoul, A.; Mikhonin, A.; Munro, C.; Asher, S. A. *Appl. Spectrosc.* **2005**, *59*, 1541.

(68) Lednev, I. K.; Ermolenkov, V. V.; He, W.; Xu, M. *Anal. Bioanal. Chem.* **2005**, *381*, 431.

(69) Balakrishnan, G.; Hu, Y.; Spiro, T. G. *Appl. Spectrosc.* **2006**, *60*, 347.

(70) Asher, S. A.; Bormett, R. W.; Chen, X. G.; Lemmon, D. H.; Cho, N.; Peterson, P.; Arrigoni, M.; Spinelli, L.; Cannon, J. *Appl. Spectrosc.* **1993**, *47*, 628.

(71) Sparrow, M. C.; Jackovitz, J. F.; Munro, C. H.; Hug, W. F.; Asher, S. A. *Appl. Spectrosc.* **2001**, *55*, 66.

(72) Holtz, J. S. W.; Bormett, R. W.; Chi, Z. H.; Cho, N. J.; Chen, X. G.; Pajcini, V.; Asher, S. A.; Spinelli, L.; Owen, P.; Arrigoni, M. *Appl. Spectrosc.* **1996**, *50*, 1459.

(73) Zhao, X. J.; Chen, R. P.; Tengroth, C.; Spiro, T. G. *Appl. Spectrosc.* **1999**, *53*, 1200.

(74) Huang, C. Y.; Balakrishnan, G.; Spiro, T. G. *J. Raman Spectrosc.* **2006**, *37*, 277.

(75) Ahmed, Z.; Scaffidi, J. P.; Asher, S. A. *Biopolymers* **2009**, *91*, 52.

(76) Kallenbach, N. R.; Lyu., P.; Zhou, H. In *Circular dichroism and conformational analysis of biomolecules*; Fasman, G. D., Ed.; Plenum Press: New York, 1996; p 201.

(77) Sharma, B.; Bykov, S. V.; Asher, S. A. *J. Phys. Chem. B* **2008**, *112*, 11762.

(78) Asher, S. A.; Chi, Z. H.; Li, P. S. *J. Raman Spectrosc.* **1998**, *29*, 927.

(79) Chen, X. G.; Asher, S. A.; Schweitzerstenner, R.; Mirkin, N. G.; Krimm, S. *J. Am. Chem. Soc.* **1995**, *117*, 2884.

(80) Myshakina, N. S.; Asher, S. A. *J. Phys. Chem. B* **2007**, *111*, 4271.

(81) Bykov, S. V.; Asher, S. A. *J. Phys. Chem. Lett.* **2010**, *1*, 269.

(82) Mikhonin, A. V.; Bykov, S. V.; Myshakina, N. S.; Asher, S. A. *J. Phys. Chem. B* **2006**, *110*, 1928.

(83) Mikhonin, A. V.; Ahmed, Z.; Ianoul, A.; Asher, S. A. *J. Phys. Chem. B* **2004**, *108*, 19020.

(84) Lednev, I. K.; Karnoup, A. S.; Sparrow, M. C.; Asher, S. A. *J. Am. Chem. Soc.* **1999**, *121*, 8074.

(85) Wang, Y.; Purrello, R.; Jordan, T.; Spiro, T. G. *J. Am. Chem. Soc.* **1991**, *113*, 6359.

(86) Mix, G.; Schweitzer-Stenner, R.; Asher, S. A. *J. Am. Chem. Soc.* **2000**, *122*, 9028.

(87) Mikhonin, A. V.; Asher, S. A. *J. Phys. Chem. B* **2005**, *109*, 3047.

(88) Chi, Z. H.; Chen, X. G.; Holtz, J. S. W.; Asher, S. A. *Biochemistry* **1998**, *37*, 2854.

(89) Sharma, B.; Asher, S. A. *J. Phys. Chem. B* **2010**, *114*, 6661.

(90) Chen, X. G.; Li, P. S.; Holtz, J. S. W.; Chi, Z. H.; Pajcini, V.; Asher, S. A.; Kelly, L. A. *J. Am. Chem. Soc.* **1996**, *118*, 9705.

(91) Asher, S. A.; Ianoul, A.; Mix, G.; Boyden, M. N.; Karnoup, A.; Diem, M.; Schweitzer-Stenner, R. *J. Am. Chem. Soc.* **2001**, *123*, 11775.

(92) Myshakina, N. S.; Ahmed, Z.; Asher, S. A. *J. Phys. Chem. B* **2008**, *112*, 11873.

(93) Oboodi, M. R.; Alva, C.; Diem, M. *J. Phys. Chem.* **1984**, *88*, 501.

(94) Ianoul, A.; Boyden, M. N.; Asher, S. A. *J. Am. Chem. Soc.* **2001**, *123*, 7433.

(95) Asher, S. A.; Mikhonin, A. V.; Bykov, S. *J. Am. Chem. Soc.* **2004**, *126*, 8433.

(96) Shi, Z.; Olson, C.; Rose, G.; Baldwin, R.; Kallenbach, N. *Proc. Natl. Acad. Sci. U. S. A.* **2002**, *99*, 9190.

(97) Mikhonin, A. V.; Myshakina, N. S.; Bykov, S. V.; Asher, S. A. *J. Am. Chem. Soc.* **2005**, *127*, 7712.

(98) Krimm, S.; Mark, J. E. *Proc. Natl. Acad. Sci. U. S. A.* **1968**, *60*, 1122.

(99) Ma, L.; Ahmed, Z.; Mikhonin, A. V.; Asher, S. A. *J. Phys. Chem. B* **2007**, *111*, 7675.

(100) Lednev, I. K.; Karnoup, A. S.; Sparrow, M. C.; Asher, S. A. *J. Am. Chem. Soc.* **2001**, *123*, 2388.

(101) Lednev, I. K.; Karnoup, A. S.; Sparrow, M. C.; Asher, S. A. *J. Am. Chem. Soc.* **1999**, *121*, 4076.

(102) Munoz, V.; Thompson, P. A.; Hofrichter, J.; Eaton, W. A. *Nature* **1997**, *390*, 196.

(103) JiJi, R. D.; Balakrishnan, G.; Hu, Y.; Spiro, T. G. *Biochemistry* **2006**, *45*, 34.

(104) Huang, C. Y.; Balakrishnan, G.; Spiro, T. G. *Biochemistry* **2005**, *44*, 15734.

(105) Balakrishnan, G.; Hu, Y.; Bender, G. M.; Getahun, Z.; DeGrado, W. F.; Spiro, T. G. *J. Am. Chem. Soc.* **2007**, *129*, 12801.

(106) Balakrishnan, G.; Hu, Y.; Case, M. A.; Spiro, T. G. *J. Phys. Chem. B* **2006**, *110*, 19877.

(107) Mikhonin, A.; Asher, S.; Bykov, S.; Murza, A. *J. Phys. Chem. B* **2007**, *111*, 3280.

(108) Balakrishnan, G.; Hu, Y.; Bender, G. M.; Getahun, Z.; DeGrado, W. F.; Spiro, T. G. *Biophys. J.* **2005**, *88*, 39A.

(109) Balakrishnan, G.; Hu, Y.; Case, M. A.; McLendon, G. A.; Spiro, T. G. *Biophys. J.* **2004**, *86*, 499A.

(110) Ianoul, A.; Mikhonin, A.; Lednev, I. K.; Asher, S. A. *J. Phys. Chem. A* **2002**, *106*, 3621.

(111) Mikhonin, A.; Asher, S. *J. Am. Chem. Soc.* **2006**, *128*, 13789.

(112) Phillips, C. M.; Mizutani, Y.; Hochstrasser, R. M. *Proc. Natl. Acad. Sci. U. S. A.* **1995**, *92*, 7292.

(113) Lian, T.; Locke, B.; Kholodenko, Y.; Hochstrasser, M. *J. Phys. Chem.* **1994**, *98*, 11648.

(114) Hashimoto, S.; Fukasaka, J.; Takeuchi, H. *J. Raman Spectrosc.* **2001**, *32*, 557.

(115) Chi, Z. H.; Asher, S. A. *Biochemistry* **1999**, *38*, 8196.

(116) Hughson, F. M.; Wright, P. E.; Baldwin, R. L. *Science* **1990**, *249*, 1544.

(117) Haruta, N.; Kitagawa, T. *Biochemistry* **2002**, *41*, 6595.

(118) Sato, A.; Mizutani, Y. *Biochemistry* **2005**, *44*, 14709.

(119) Sanchez, K. M.; Neary, T. J.; Kim, J. E. *J. Phys. Chem. B* **2008**, *112*, 9507.

(120) El-Mashtoly, S. F.; Yamauchi, S.; Kumauchi, M.; Hamada, N.; Tokunaga, F.; Unno, M. *J. Phys. Chem. B* **2005**, *109*, 23666.

(121) Kim, J. E.; Pan, D. H.; Mathies, R. A. *Biochemistry* **2003**, *42*, 5169.

(122) Kaminaka, S.; Mathies, R. A. *Laser Chem.* **1999**, *19*, 165.

(123) Chen, J.; Barry, B. A. *Photochem. Photobiol.* **2008**, *84*, 815.

(124) Chen, J.; Bender, S. L.; Keough, J. M.; Barry, B. A. *J. Phys. Chem. B* **2009**, *113*, 11367.

(125) Okishio, N.; Fukuda, R.; Nagai, M.; Nagai, Y.; Nagatomo, S.; Kitagawa, T. *J. Raman Spectrosc.* **1998**, *29*, 31.

(126) Simpson, J. V.; Oshokoya, O.; Wagner, N.; Liu, J.; JiJi, R. D. *Analyst* **2011**, *136*, 1239.

(127) Simpson, J. V.; Balakrishnan, G.; JiJi, R. D. *Analyst* **2009**, *134*, 138.

(128) Halsey, C. M.; Oshokoya, O. O.; Jiji, R. D.; Cooley, J. W. *Biochemistry* **2011**, *50*, 6531.

(129) Halsey, C. M.; Xiong, J.; Oshokoya, O. O.; Johnson, J. A.; Shinde, S.; Beatty, J. T.; Ghirlanda, G.; JiJi, R. D.; Cooley, J. W. *ChemBioChem* **2011**, *12*, 2125.

(130) Couling, V. W.; Foster, N. W.; Klenerman, D. *J. Raman Spectrosc.* **1997**, *28*, 33.

(131) Pieridou, G. K.; Hayes, S. C. *Phys. Chem. Chem. Phys.* **2009**, *11*, 5302.

(132) Lednev, I. K.; Shashilov, V.; Xu, M. *Curr. Sci.* **2009**, *97*, 180.

(133) Xu, M.; Ermolenkov, V. V.; Uversky, V. N.; Lednev, I. K. *J. Biophotonics* **2008**, *1*, 215.

(134) Lednev, I.; Kurouski, D.; Lauro, W. In *Amyloid Fibrils are "Alive" as Evident from Deep UV Raman Spectroscopic Examination: an Intrumentation Driven Approach*; 2010; p 172.

(135) Popova, L. A.; Kodali, R.; Wetzel, R.; Lednev, I. K. *J. Am. Chem. Soc.* **2010**, *132*, 6324.

(136) Shashilov, V.; Xu, M.; Ermolenkov, V. V.; Fredriksen, L.; Lednev, I. K. *J. Am. Chem. Soc.* **2007**, *129*, 6972.

(137) Shashilov, V. A.; Lednev, I. K. *J. Am. Chem. Soc.* **2008**, *130*, 309.

(138) Shashilov, V. A.; Lednev, I. K. *J. Raman Spectrosc.* **2009**, *40*, 1749.

(139) Shashilov, V. A.; Lednev, I. K. *Chem. Rev.* **2010**, *110*, 5692.

(140) Shashilov, V. A.; Sikirzhytski, V.; Popova, L. A.; Lednev, I. K. *Methods* **2010**, *52*, 23.

(141) Sikirzhytski, V.; Topilina, N. I.; Higashiya, S.; Welch, J. T.; Lednev, I. K. *J. Am. Chem. Soc.* **2008**, *130*, 5852.

(142) Xu, M.; Shashilov, V.; Lednev, I. K. *J. Am. Chem. Soc.* **2007**, *129*, 11002.

(143) Brereton, R. G. *Chemometrics: Data Analysis for the Laboratory and Chemical Plant*. Wiley: Chichester, U.K., 2003; p 489.

(144) Hyvarinen, A.; Karhunen, J.; Oja, E., *Independent Component Analysis*; John Wiley & Sons Inc.: New York, 2002; pp 145−164.

(145) Hyvarinen, A.; Hoyer, P. O.; Inki, M. *Neural Comput.* **2001**, *13*, 1527.

(146) Shao, X. G.; Wang, G. Q.; Wang, S. F.; Su, Q. D. *Anal. Chem.* **2004**, *76*, 5143.

(147) Cichocki, A.; Amari, S. I. *Adaptive Blind Signal and Image Processing: Lerning Algorithms and Applications*; John Wiley: Chichester, U.K., New York, 2002; p 554.

(148) Cichocki, A.; Amari, S. I., *Adaptive Blind Signal and Image Processing: Learning Algorithms and Applications*; John Wiley: Chichester, U.K., New York, 2002; p 554.

(149) Bell, A. J.; Sejnowski, T. J. *Neural Comput.* **1995**, *7*, 1129.

(150) Hyvarinen, A.; Oja, E. *Neural Networks* **2000**, *13*, 411.

(151) Noda, I.; Ozaki, Y. *Two-Dimensional Correlation Spectroscopy: Applications in Vibrational and Optical Spectroscopy*; John Wiley & Sons: Chichester, U.K., Hoboken, NJ, 2004.

(152) Shanmukh, S.; Dluhy, R. A. *J. Phys. Chem. A* **2004**, *108*, 5625.

(153) Xu, M.; Shashilov, V. A.; Ermolenkov, V. V.; Fredriksen, L.; Zagorevski, D.; Lednev, I. K. *Protein Sci.* **2007**, *16*, 815.

(154) Artymiuk, P. J.; Blake, C. C. F.; Rice, D. W.; Wilson, K. S. *Acta Crystallogr., Sect. B: Struct. Sci.* **1982**, *38*, 778.

(155) Booth, D. R.; Sunde, M.; Bellotti, V.; Robinson, C. V.; Hutchinson, W. L.; Fraser, P. E.; Hawkins, P. N.; Dobson, C. M.; Radford, S. E.; Blake, C. C. F.; Pepys, M. B. *Nature* **1997**, *385*, 787.

(156) Englander, S. W.; Sosnick, T. R.; Englander, J. J.; Mayne, L. *Curr. Opin. Struct. Biol.* **1996**, *6*, 18.

(157) DeFlores, L. P.; Tokmakoff, A. *J. Am. Chem. Soc.* **2006**, *128*, 16520.

(158) Knuth, K. H. *SPIE* **1998**, *3459*, 147.

(159) Topilina, N. I.; Ermolenkov, V. V.; Higashiya, S.; Welch, J. T.; Lednev, I. K. *Biopolymers* **2007**, *86*, 261.

(160) Topilina, N. I.; Ermolenkov, V. V.; Sikirzhytski, V.; Higashiya, S.; Lednev, I. K.; Welch, J. T. *Biopolymers* **2010**, *93*, 607.

(161) Topilina, N. I.; Higashiya, S.; Rana, N.; Ermolenkov, V. V.; Kossow, C.; Carlsen, A.; Ngo, S. C.; Wells, C. C.; Eisenbraun, E. T.; Dunn, K. A.; Lednev, I. K.; Geer, R. E.; Kaloyeros, A. E.; Welch, J. T. *Biomacromolecules* **2006**, *7*, 1104.

(162) Topilina, N. I.; Sikirzhytsky, V.; Higashiya, S.; Ermolenkov, V. V.; Lednev, I. K.; Welch, J. T. *Biomacromolecules* **2010**, *11*, 1721.

(163) Lednev, I. K.; Ermolenkov, V. V.; Higashiya, S.; Popova, L. A.; Topilina, N. I.; Welch, J. T. *Biophys. J.* **2006**, *91*, 3805.

(164) Swint, L.; Robertson, A. D. *Protein Sci.* **1993**, *2*, 2037.

(165) Windig, W.; Gallagher, N. B.; Shaver, J. M.; Wise, B. M. *Chemom. Intell. Lab. Syst.* **2005**, *77*, 85.

(166) Petkova, A. T.; Ishii, Y.; Balbach, J. J.; Antzutkin, O. N.; Leapman, R. D.; Delaglio, F.; Tycko, R. *Proc. Natl. Acad. Sci. U. S. A.* **2002**, *99*, 16742.

(167) Wang, M.; JiJi, R. D. *J. Biophotonics* **2011**, *4*, 637.

(168) Baskakov, I. V. In *Amyloid Proteins: The Beta Sheet Conformation and Disease*; Sipe, J. D., Ed.; Wiley-VCH: Weinheim, Germany, 2005.

(169) Wolf, M. G.; Gestel, J.; de Leeuw, S. W. *Methods Mol. Biol.* **2008**, *474*, 153.

(170) Brange, J.; Andersen, L.; Laursen, E. D.; Meyn, G.; Rasmussen, E. *J. Pharm. Sci.* **1997**, *86*, 517.

(171) Kim, H. Y.; Cho, M. K.; Riedel, D.; Fernandez, C. O.; Zweckstetter, M. *Angew. Chem., Int. Ed.* **2008**, *47*, 5046.

(172) Kurouski, D.; Lauro, W.; Lednev, I. K. *Chem. Commun.* **2010**, *46*, 4249.